

Binary Black Hole Waveforms from High-Resolution GR-Athena++ Simulations

Alireza Rashti^{1,2,3}, Rossella Gamba^{1,2,3,4}, Koustav Chandra^{1,2,3}, David Radice^{1,2,3}, Boris Daszuta⁵, William Cook⁵, and Sebastiano Bernuzzi⁵

¹ *Institute for Gravitation and the Cosmos, The Pennsylvania State University, University Park, PA 16802, USA*

² *Department of Physics, The Pennsylvania State University, University Park, PA 16802, USA*

³ *Department of Astronomy & Astrophysics, The Pennsylvania State University, University Park, PA 16802, USA*

⁴ *Department of Physics, University of California, Berkeley, CA 94720, USA and*

⁵ *Theoretisch-Physikalisches Institut, Friedrich-Schiller-Universität Jena, 07743, Jena, Germany*

The detection and subsequent inference of binary black hole signals rely heavily on the accuracy of the waveform model employed. In the highly non-linear, dynamic, and strong-field regime near merger, these waveforms can only be accurately modeled through numerical relativity simulations. Considering the precision requirements of next-generation gravitational wave observatories, we present in this paper high-resolution simulations of four non-spinning quasi-circular binary black hole systems with mass ratios of 1, 2, 3, and 4, conducted using the **GR-Athena++** code. We extract waveforms from these simulations using both finite radius and Cauchy characteristic extraction methods. Additionally, we provide a comprehensive error analysis to evaluate the accuracy and convergence of the waveforms. This dataset encompasses gravitational waves of the precision (self-mismatch) demanded by upcoming gravitational detectors such as LISA, Cosmic Explorer, and Einstein Telescope. The waveforms are publicly available on ScholarSphere [1–4], and represent the first set of waveforms of the new **GR-Athena++** catalog.

I. INTRODUCTION

The field of numerical relativity (NR) achieved a major milestone in 2005 by successfully simulating binary black hole (BBH) systems with comparable masses through the stages of inspiral, merger, and ringdown [5–7]. This accomplishment resulted from decades of work, beginning with Hahn and Lindquist in the 1960s [8], and involving contributions from numerous groups over the years. Today, several advanced codes, built on diverse numerical techniques and formulations, can robustly evolve BBH mergers and extract the resulting gravitational waves (GWs) [7, 9–21].

NR simulations of the late-inspiral, merger, and ringdown phases of BBHs play a critical role in constructing and validating accurate waveform models used in GW data analysis. These models are essential for tasks such as signal detection and parameter estimation. In particular, NR simulations serve as the foundation for creating semi-analytic waveform models, including the effective-one-body (EOB) [22–32] and phenomenological inspiral-merger-ringdown (IMR) models [33–49], as well as for developing NR-based interpolants like the surrogate models [50–54]. Additionally, NR simulations have been used to assess the sensitivity of searches to binary populations and to establish upper limits on merger rate density, particularly for intermediate-mass black hole (IMBH) binaries [55–57].

Therefore, the accuracy of these NR simulations is a critical factor that constrains the precision of the waveform models used in GW analysis. As detector sensitivity continues to improve, with current instruments like Advanced LIGO [58] reaching new levels in their fourth observing run, and with the advent of next-generation (XG) GW detectors such as the Cosmic Explorer (CE) [59, 60] and Einstein Telescope (ET) [61, 62], which are antic-

ipated to be at least ten times more sensitive, the demand for even more accurate waveform models becomes increasingly urgent. Future space-based missions, such as LISA [63], TianQin [64], Taiji [65], DECIGO [66], and the Lunar Gravitational-Wave Antenna (LGWA) [67] will further heighten this need.

Although quantifying the exact degree of accuracy required for upcoming detectors is challenging, numerous studies have shown that the precision of current state-of-the-art waveforms must be significantly enhanced to avoid biased source parameter estimates [68–71]. Reference [72] studied these accuracy requirements for BBH systems observed by ET and CE, concluding that simulations must improve by approximately one or more orders of magnitude to meet the demands of the XG detectors. Similarly, Ref. [73] and Ref. [74] recently evaluated the impact of finite grid resolution on NR waveform precision, emphasizing the need for higher-resolution NR simulations, especially for CE and LISA.

Beyond studies assessing the accuracy improvement of simulations from the same catalogs, cross-comparisons between simulations obtained with different codes and techniques [56, 75, 76] also play a crucial role in validating the robustness of the resulting waveforms. To this end, the production of new, high-resolution NR simulations is crucial.

In this work, we use **GR-Athena++** [21, 77] to conduct high-resolution dynamical evolutions of non-spinning, quasi-circular BBH systems with varying mass ratios. The total computational cost of these BBH simulations is ~ 155 million core-hours. *They constitute the first waveforms in the GR-Athena++ catalog [1–4]*, simulated with the aim of meeting the precision requirements of future GW detectors. Their accuracy is thoroughly assessed through a series of tests, including direct comparisons with selected waveforms from the SXS catalog, provid-

ing robust cross-validation with prior results.

The rest of this paper is structured as follows. In Sec. II, we provide a detailed overview of the numerical methods, including grid configurations, GW extraction techniques, and error estimation models. In Sec. III we present our simulations, showcasing the waveforms for different modes along with the trajectories of the BBH systems for each mass ratio. Sec. III is dedicated to evaluating the quality of the waveforms through a series of convergence studies and cross-validation against waveforms from the SXS catalog. Specifically, we analyse the convergence of Cauchy characteristic extraction (CCE) strains and estimate their errors contributed from different parameters such as the resolution and world tube extraction radius. Comparisons against SXS are performed via time-domain alignment as well as frequency-domain mismatch calculations, considering both single-mode and multi-mode waveforms. Finally, Sec. IV concludes our work with an overview of our results and reflections on future research directions. Additional material for further examination is provided in the appendices.

Throughout the paper, we use geometrized units where $G = c = 1$, with G representing the gravitational constant and c the speed of light.

II. NUMERICAL SIMULATIONS

A. Numerical methods

We conduct NR simulation of BBH systems with `GR-Athena++`. This framework computes spatial derivatives using a sixth-order finite difference scheme, resulting in a truncation error of $\mathcal{O}(\delta x^6)$, where δx denotes the grid spacing. To control numerical noise, we employ an eighth-order Kreiss-Oliger dissipation operator with $\epsilon = 0.5$, thereby introducing an error of $\mathcal{O}(\delta x^7)$. Time integration is performed using a fourth-order Runge-Kutta method, incurring an error of $\mathcal{O}(\delta x^4)$ during extended time evolutions. Additionally, we maintain a Courant-Friedrichs-Lewy factor of 0.25 to ensure numerical stability throughout the simulations.

For simulating the BBH systems, we use the Z4c formulation of Einstein’s equation [78, 79] and set the gauges of the system using the moving puncture gauge conditions as specified in Ref. [21].

B. Grid setup

To enhance computational speed through parallelization, we divide the computational grid (numerical domain) in `GR-Athena++` into multiple subdomains called `MeshBlocks` [21, 80].

The resolution of the root (or base) grid is determined by specifying the number of grid points in each direction. We divide the root grid into `MeshBlocks`, each containing a predetermined number of grid points that must

be a divisor of the total points in the root grid. These `MeshBlocks` are recursively subdivided to create the full adaptive mesh refinement octree structure grid, starting from the root grid.

For adaptive mesh refinement, we employ the L_2 refinement method introduced in [77], in which finer grid levels centre around each BH, coarsening gradually toward the outer boundary based on an L_2 -norm criterion. As demonstrated in [77], this L_2 method yields a grid structure similar to the “sphere-in-sphere” Berger-Oliger algorithm [81], but without overlapping `MeshBlocks`.

The L_2 method provides both speed and accuracy benefits over the originally implemented L_∞ method [21]. By employing the L_2 method, which generates fewer `MeshBlocks`, we achieve an efficient grid structure as the sphere-like configurations from the L_2 method fit more efficiently within the box structures generated by the L_∞ method.

In our simulations, the `MeshBlock`’s size, in all directions, is set to 16. The number of refinement levels, set between 12 and 14, is chosen based on the BBH’s mass ratio, to ensure a minimum resolution of $m_2/\delta x > 25$ at the lowest resolution of the root grid, where m_2 is the mass of lighter or secondary BH and δx is the grid spacing at the puncture.

We use Sommerfeld boundary conditions [79] at the outer boundary of the computational grid. These boundary conditions are imperfect, and may cause reflection of nonphysical modes into the domain. To mitigate this, we use a sufficiently large domain so that the largest waveform extraction radius is causally disconnected from the outer boundary.

Lastly, as all considered binaries exhibit reflection symmetry across the orbital plane, we only evolve the region above the orbital plane ($z > 0$) and impose bitant symmetry at the $z = 0$ boundary.

C. Initial data

We start our simulations by generating BBH puncture initial data using the pseudo-spectral elliptic solver `TwoPunctures` code [82]. We place the BHs along the x -axis at a distance D apart, such that the center of mass of each system with mass ratio $q = m_1/m_2 \geq 1$ is at the origin. The `TwoPunctures` code estimates the component masses m_1 and m_2 such that the total mass of the binary satisfies $m_1 + m_2 = 1$. We use the separation distance D and the momentum components along the x and y directions, P_x and P_y , from [83, 84]. This ensures low-eccentricity initial data, producing approximately 20 quasi-circular pre-merger cycles for the $q = 1$ system and around 15 pre-merger cycles for $q = 2$, $q = 3$, and $q = 4$ systems. Table (I) summarizes these initial data parameters for our simulations.

q	D/M	$10^4 \times P_x/M $	$10^2 \times P_y/M $	N	$10^3 \times \delta x/M$
1	12	4.681	8.507	128, 192, 256, 320, 384	19.65, 13.10, 9.83, 7.86, 6.55
2	10	7.948	8.560	128, 192, 256, 320, 384	5.981, 3.988, 2.991, 2.393, 1.994
3	10	4.968	7.237	128, 192, 256, 320, 384	6.775, 4.517, 3.387, 2.710, 2.258
4	10	4.211	6.188	128, 192, 256, 320	3.723, 2.482, 1.862, 1.489

TABLE I. Parameters of BBH simulations. q denotes the mass ratio, and D is the distance between two BBHs. $|P_x/M|$ and $|P_y/M|$ respectively denote x and y momentum components of the BHs in the `TwoPunctures` initial data code. The total mass of the system $M = 1$ in all cases. Each mesh block contains 16^3 grid points. The mesh resolution N specifies the number of grid points on the root grid in each direction while the grid space, δx , indicates the resolutions at the finest level.

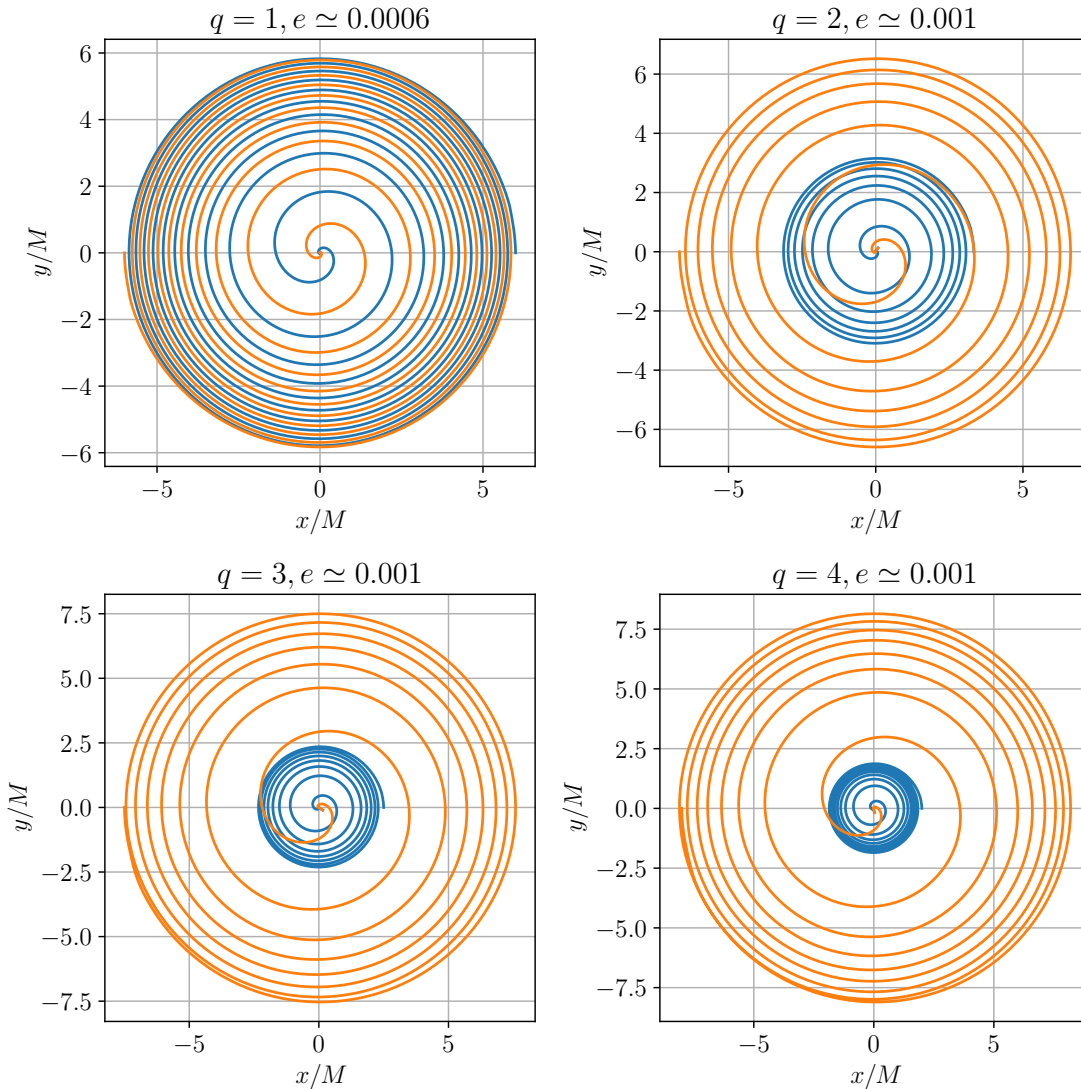


FIG. 1. Quasi-circular orbits of BBH simulations. The orbits are drawn by tracking the coordinate of each puncture. The mass ratio and eccentricity of each run is specified. The eccentricity (e) approximated based on a fit to the coordinate distance for the first few orbits of the run, see the text.

D. Gravitational waves

To compute waveforms at null infinity \mathcal{I}_+ , we use either an approximate method based on post-Newtonian theory (finite radius extraction; FRE), or the CCE method. The latter directly solves Einstein's equations to \mathcal{I}_+ , and

therefore represents our preferred technique for computing gravitational waves (GWs). We describe it in detail in this section. Additional information regarding the FRE method can be found in App. (A), while App. (D) collects comparisons of data obtained with the two methods to evaluate their systematic uncertainties.

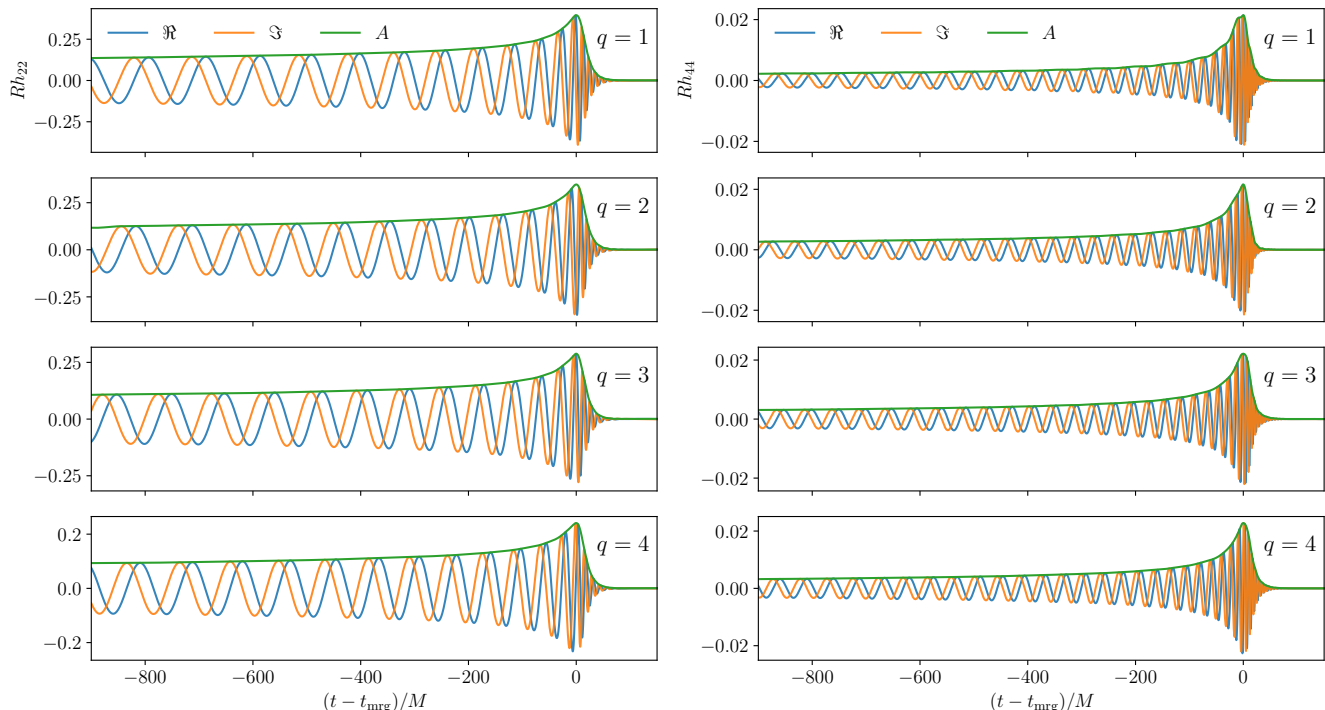


FIG. 2. This figure shows the real and the imaginary parts of (2, 2) [left] and (4, 4) [right] multipoles of the CCE strains for our simulations. We also show the amplitude evolution of these modes. t_{mrg} is defined as the peak amplitude time of the (2, 2) mode.

To generate GWs at \mathcal{I}_+ using the publicly available PITTNull code [16, 85], we develop a pipeline that generates the necessary input data. This pipeline expands the metric fields—specifically the spatial metric γ_{ij} , the shift vector $\vec{\beta}$, and the lapse α —in the 3+1 formalism [86] over a defined radial range $[r_1, r_2]$. Each metric field \mathcal{G} is expanded as follows:

$$\mathcal{G}(t, x^i) = \sum_{k=0}^{k_{\text{max}}} \sum_{l=0}^{l_{\text{max}}} \sum_{m=-l}^l C_{klm}(t) U_k(\tau(r)) Y_{lm}(\theta, \phi), \quad (1)$$

where, $U_k(\tau)$ are Chebyshev polynomials of the second kind, $Y_{lm}(\theta, \phi)$ are spherical harmonic basis functions, and

$$\tau(r) := \frac{2r - r_1 - r_2}{r_2 - r_1}. \quad (2)$$

For this study, we use $k_{\text{max}} = l_{\text{max}} = 11$. The expansion coefficients C_{klm} are computed every 20th to 30th time steps during the evolution and stored in an `hdf5` file to serve as boundary condition samples on concentric world tubes for the PITTNull code.

App. (E) shows, as an example, the C_{222} coefficients for γ_{xx} . The presence of noise in the C_{klm} coefficients at the beginning of the run and even at a later times is one of the challenges to deal with when computing CCE strains. We have tested different filtering methods to address this

issue, as detailed in App. (E), but ultimately chose not to filter C_{klm} when computing the presented waveforms.

We can use the Weyl curvature scalar $\psi_4^{\ell m}$ or the News function $N_4^{\ell m}$ to compute strains as the PITTNull code computes both. These are related to the GW strain as:

$$\psi_4^{\ell m} = \ddot{h}_+^{\ell m} - i\dot{h}_\times^{\ell m}, \quad N_4^{\ell m} = \dot{h}_+^{\ell m} - i\dot{h}_\times^{\ell m}, \quad (3)$$

where the dots indicate time derivatives. In both scenarios, the initial step involves normalizing the quantities by multiplying them by a factor of $2 \times (-1)^{l+m}$. To recover the strain from either, we use the fixed frequency integration (FFI) method [87]. The cutoff frequency employed for this process is given in App. (B).

E. Uncertainty quantification

We estimate the finite-resolution and finite-extraction radius errors in our NR simulations by performing a series of convergence studies on the strain data obtained using CCE, as discussed in Sec. III B, and FRE, as detailed in App. (C). In both cases, we model the error in any numerically computed quantity w as a power of δ [88, 89]

$$w(\delta) = w_{\text{ex}} + c_n \delta^n + \mathcal{O}(\delta^{n+1}). \quad (4)$$

Here, w_{ex} represents the exact value of w . The parameter δ can be N^{-1} , where N is the number of grid

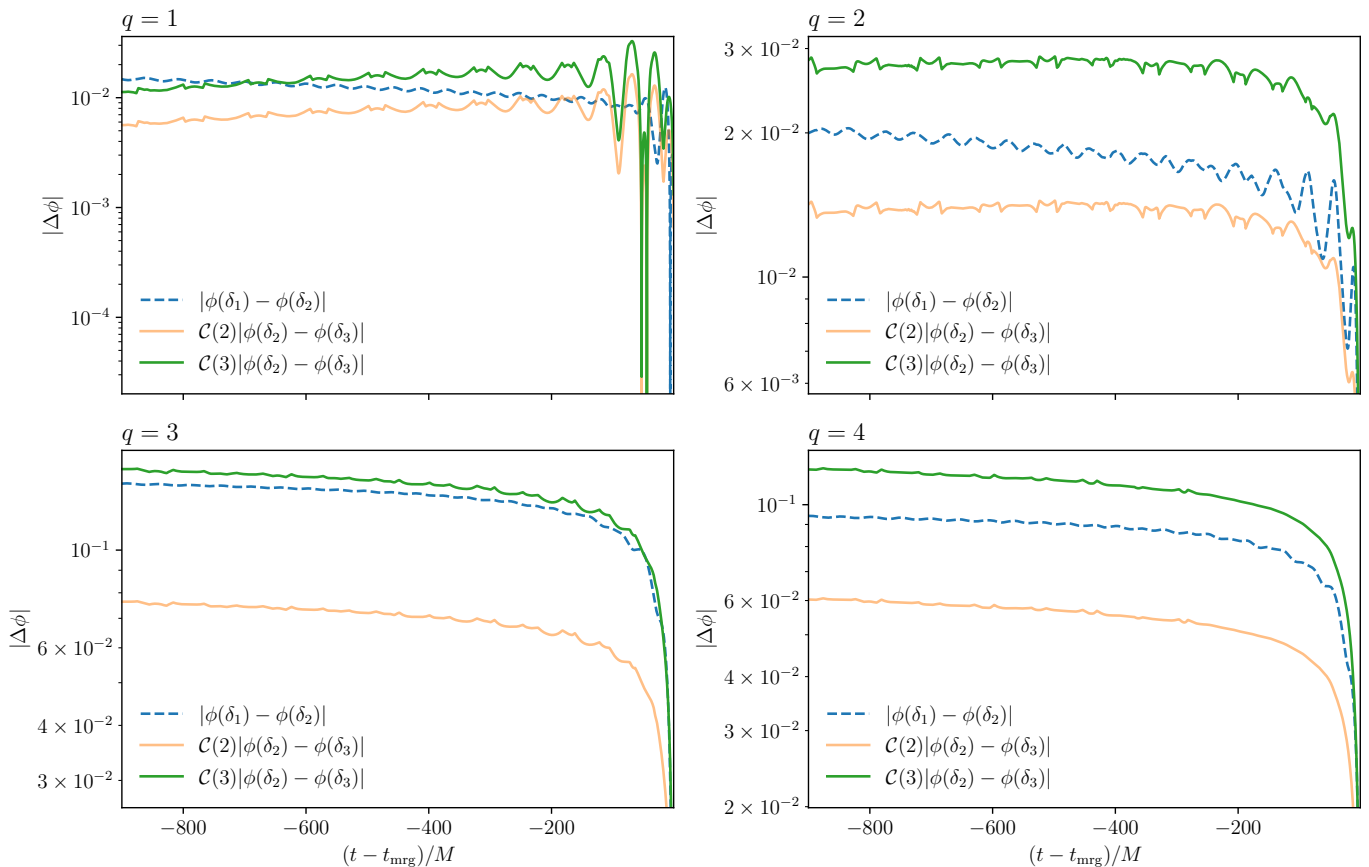


FIG. 3. Convergence of CCE strains, (2,2) modes. Here, we have $\delta_i^{-1} \in [56, 112, 224]$ for $i = 1, 2, 3$. The strains are computed from $\psi_4^{\ell m}$. The boundary condition for PITTNull is obtained by the highest resolution from the table (I) and the radius of world tube extraction is 50. The strains show $\gtrsim 2$ nd order of convergence for $q = 1, 2$, and 4 runs, while the strain of $q = 3$ run exhibits ~ 3 rd order of convergence. Nevertheless, in our error analyses, we choose 2nd order convergence rate for all strains with respect to the PITTNull's resolution, expected from the PITTNull code [16].

points on the root grid of the simulation when evaluating finite-resolution errors; δ can also be R^{-1} , where R is the extraction radius, when assessing finite extraction-radius effects. The coefficient c_n quantifies the amplitude of the leading-order error term. Note that in Equation Eq. (4), no summation is implied over the same indices.

To estimate the convergence order, we exploit the difference in w obtained at various δ 's

$$|w(\delta_1) - w(\delta_2)| - \mathcal{C}(n)|w(\delta_2) - w(\delta_3)|, \quad (5)$$

where $\mathcal{C}(n)$ is defined

$$\mathcal{C}(n) = \left| \frac{\delta_1^n - \delta_2^n}{\delta_2^n - \delta_3^n} \right|. \quad (6)$$

By minimizing Eq. (5) with respect to n , we infer the value of n that characterizes the optimal convergence rate.

Moreover, for a specific δ , for instance, $w(\delta_2)$, we can estimate the magnitude of the leading order error, i.e.,

$|c_n \delta^n|$, using

$$\left| \frac{w(\delta_1) - w(\delta_2)}{1 - \left(\frac{\delta_1}{\delta_2}\right)^n} \right|. \quad (7)$$

If no convergence is observed for a specific study, we use $n = 0$; in these cases, the error is estimated by $|w(\delta_1) - w(\delta_2)|$.

For example, when evaluating finite-resolution errors pertinent to the GR-Athena++ resolution, $\delta = N^{-1}$ and N can take values such as 128, 192, 256, 320, and 384 (see Table I). Once we determine n , by minimizing Eq. (5), and c_n , by using Eq. (7) we can quantify the leading-order error term, namely $c_n \delta^n$, for each given resolution. Similarly, when assessing finite extraction-radius effects, R can assume values like 20, 50, and 100, allowing us to estimate the error associated with the radius of the world tube in the waveforms.

Lastly, in our convergence studies, after the initial junk radiation, i.e., Brill waves [89, 90], we observe some dephasing between different resolutions of the same run. Therefore, we align the waveforms in terms of phase and

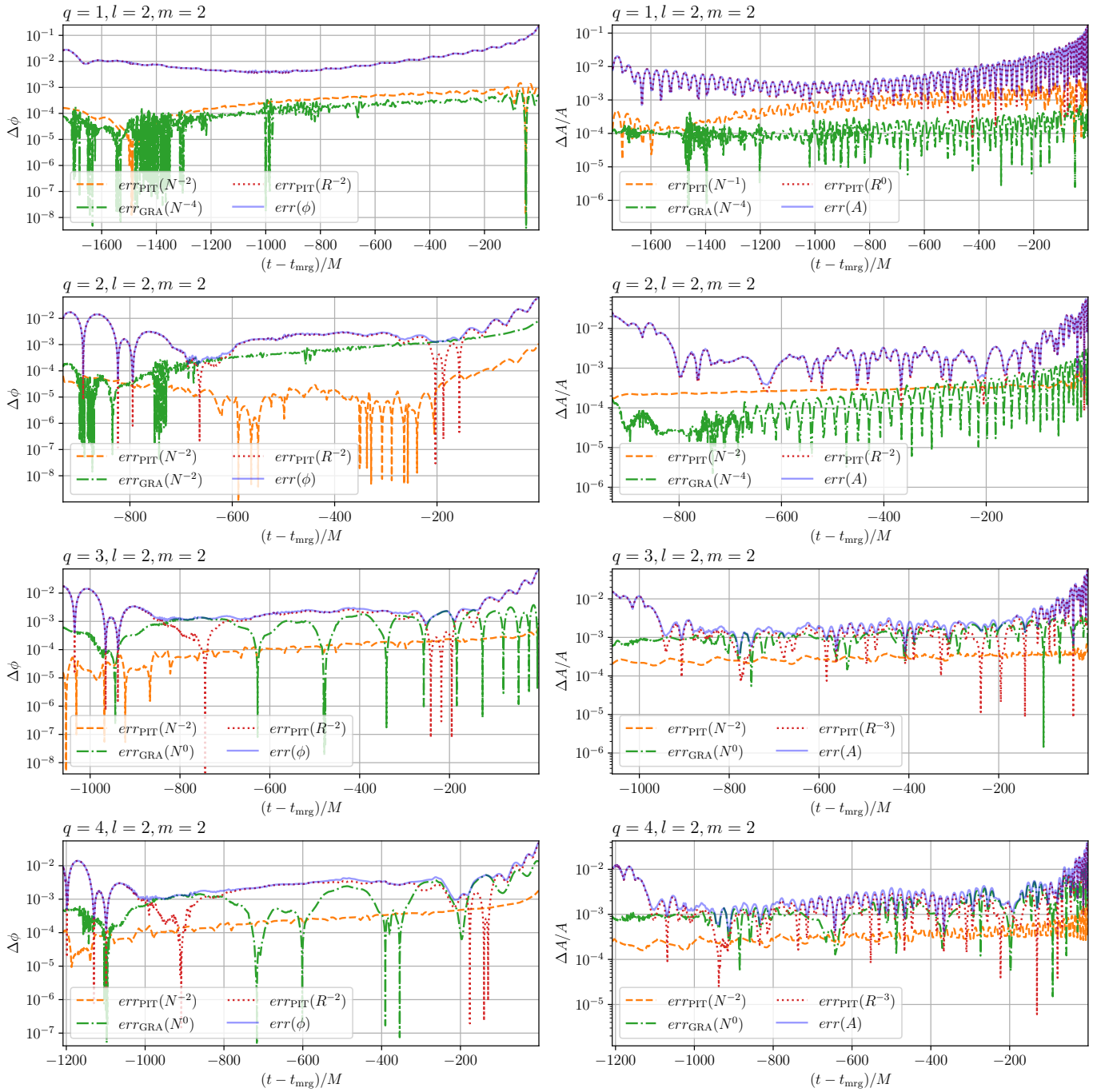


FIG. 4. Sum of errors in CCE strains (computed from $\psi_4^{\ell m}$). $err_{\text{PIT}}(N^{-p})$ denotes the error for different resolutions of the PITNull code, and p is the convergence order $err_{\text{PIT}}(R^{-p})$ is the error for different world tube radii of the PITNull code; $err_{\text{GRA}}(N^{-p})$ shows error pertinent to GR-Athena++'s resolutions. The total error err for ϕ and amplitude relative difference $\Delta A/A$ is computed by $err = (err_{\text{PIT}}^2(N^{-p}) + err_{\text{PIT}}^2(R^{-p}) + err_{\text{GRA}}^2(N^{-p}))^{1/2}$.

time at the maximum amplitude peak. This ensures that all waveforms reach their maximum amplitude simultaneously and share the same phase value. This alignment is essential for conducting convergence analysis across different extraction radii, as the timing of the maximum peak varies.

III. RESULTS

A. Simulations

After constructing the initial data of our BBH systems using the TwoPunctures code, as explained in

II C, we dynamically evolve the BBH systems using the `GR-Athena++` code.

The total simulation times chosen for each mass ratio are as follows: $q = 1$ with the total time ~ 2370 , $q = 2$ with the total time ~ 1370 , $q = 3$ with the total time ~ 1566 , and $q = 4$ with the total time ~ 1745 . The computational cost of these 19 simulations, table (I), was approximately 155 million core-hours, with a code speed of about 8×10^7 zone-cycle updates per second. This includes significant file system operations required to store the C_{klm} coefficients of Eq. (1), which are necessary for computing the CCE strains.

The trajectories for each puncture, $\vec{x}_p(t)$, are found by solving the ordinary differential equation $\dot{\vec{x}}_p(t) = -\vec{\beta}_p(t)$, in which, $\vec{\beta}_p(t)$ denotes the shift vector at the puncture [7, 21]. We estimate the eccentricity of our simulations shown in Fig. 1 using the methods discussed in [91]. This approach requires us to identify parameters, including eccentricity, to fit the coordinate distance between punctures, derived from the trajectories $\vec{x}_p(t)$, as a function of evolution time. We use the initial orbital angular velocity and the first few orbits of the simulation to find a fit for the coordinate distance versus time. We choose the coordinate distance and not its time derivative, as done in [92], because the time derivative of the coordinate distance can introduce noise. In particular, we use ~ 4 orbits and calculate the initial orbital velocity using the initial momenta and distance between the puncture, see App. (B). Specifically, BBH runs with $q = 2, 3, 4$ have an eccentricity of $\sim 10^{-3}$, and the $q = 1$ case has an eccentricity of $\sim 6 \times 10^{-4}$.

Fig. (2) shows the ($\ell = 2, m = 2$) and ($\ell = 4, m = 4$) modes of the CCE strains for our simulations. To ensure that the merger happens at $t = 0$, we subtract the merger time t_{mrg} , defined as the peak amplitude time of the (2, 2) mode, in the time axis. At t_{mrg} , a highly excited BH is formed, which then settles down to its stationary Kerr state by emitting GWs. In Fig. (2), we see each system exhibits a clear inspiral phase, followed by a merger and a ringdown. The subdominant (4, 4) mode also captures these key features, albeit with a smaller amplitude.

B. CCE error analysis

After computing the CCE strains from $\psi_4^{\ell m}$, using FFI (App. (B)), we want to determine the convergence order, and hence finding an estimate of the error budget in the waveforms.

As described earlier in Sec. (IID), we save $C_{klm}(t)$ coefficients at different radii during `GR-Athena++` evolution run, and then we deploy the `PITTNu11` code using the boundary condition samplings provided by the $C_{klm}(t)$ coefficients to solve the CCE equations. As such, we have 3 sources that contribute to the error budget: the resolution of `PITTNu11` runs, the world tube radius used to compute $C_{klm}(t)$ coefficients, and the resolution of the evolution run in `GR-Athena++` (which affects the bound-

ary condition for `PITTNu11`). We study the effect of these sources separately, and find the total error in CCE waveforms by summing the errors in quadrature.

To find the errors due to the `PITTNu11` resolution and the `PITTNu11` world tube radius, we use the $C_{klm}(t)$ data belonging to the highest available resolution of `GR-Athena++` for each mass ratio, and with various extraction tube radii, i.e., 20, 50, and 100. Then, for each radius, we run `PITTNu11` for three different resolutions with a time step corresponding to that resolution, as outlined in [16]. Specifically, we use the resolution $224 \times 200 \times 200$ with the time step Δt , the resolution $112 \times 100 \times 100$ with the time step $\Delta t/2$, and the resolution $56 \times 50 \times 50$ with the time step $\Delta t/4$. Here, the resolution is denoted by $N_r \times N_p \times N_q$, in which r is the radial direction and (p, q) are the stereographic coordinates in `PITTNu11`. Δt is the writing time of $C_{klm}(t)$, i.e., 20-th to 30-th of `GR-Athena++` evolution time, mentioned in Sec. (IID).

We first find the convergence order with respect to the `PITTNu11` resolution. Accordingly, we use Eq. (5) with $\delta = N^{-1}$, where N refers to the N_r resolution of `PITTNu11` runs. Fig. (3) depicts the convergence of CCE strain's phase computed from $\psi_4^{\ell m}$ with a world tube radius of 50¹. We observe a 2nd order convergence with respect to the `PITTNu11` resolution. Similarly, we conduct a similar convergence study for CCE strain's amplitude and find a 2nd order convergence in all runs except $q = 1$ that exhibits a 1st order convergence.

For the convergence order with respect to the `PITTNu11` extraction world tube, we use the highest resolution of `GR-Athena++` and `PITTNu11`, and use Eq. (5) with $\delta = R^{-1}$, in which R refers to the world tube radius extraction of 20, 50, and 100. The result of this convergence study shows that the CCE strain's phase demonstrates a consistent 2nd order convergence for all mass ratios. However, the amplitude converges in different orders for different mass ratios. In particular, the amplitude in $q = 1$ shows no convergence, $q = 2$ converges with a 2nd order rate, and $q = 3$ and 4 converge with a 3rd order rate.

Assessing the error budget of the waveforms due to `GR-Athena++`, we first need to find the convergence order with respect to `GR-Athena++` resolutions. As such, we run `PITTNu11` for three $C_{klm}(t)$ data which correspond to three resolutions from table (I). Specifically, we choose `GR-Athena++` resolutions of 384, 256, 128 for $q = 1, 2, 3$, and 320, 256, 128 for $q = 4$, to see a clear convergence pattern. Then, we run `PITTNu11` with the resolution $224 \times 200 \times 200$ and the time step Δt with the world tube radius of 50 for each given `GR-Athena++` resolution. Lastly, we use Eq. (5) with $\delta = N^{-1}$ to find the convergence order, where N denotes the selected `GR-Athena++`

¹ Among different world tube extraction radii, only radius = 50 exhibits convergence behavior with respect to `PITTNu11` resolutions.

resolutions. We find that $q = 1$ and $q = 2$ runs, respectively, show a 4th order convergence and a 2nd order convergence in the phase, while the higher mass ratio runs of $q = 3$ and $q = 4$ do not converge with respect to the GR-Athena++ resolutions. Similarly, for mass ratio runs of $q = 1$ and 2, the amplitude shows a 4th order convergence, while the higher mass ratios do not converge.

Having found all convergence orders, now we can use Eq. (7) to estimate the errors associated with each source, namely, the PITTNull resolution, the extraction world tube radius, and the GR-Athena++ resolution. As such, we subtract the phases and the amplitudes of two different CCE strains (different in resolution or extraction radius) in the time domain to compute the numerator of Eq. (7). To carry out this subtraction, we first align the strains and then calculate their phase and amplitude differences. The alignment is done by finding a global time and phase shift ($\Delta\phi_{22}, \Delta t$) such that

$$\chi^2 = \int_{t_i}^{t_f} [\phi_{h_1}(t + \Delta t) - \phi_{h_2}(t) - \Delta\phi_{22}]^2 dt, \quad (8)$$

is minimized. In Eq. (8), ϕ_{h_1}, ϕ_{h_2} are the $(\ell, m) = (2, 2)$ GW phases of the two waveforms (h_1, h_2) to be compared and (t_i, t_f) specify the time window over which the minimization is performed. We place the time window after the junk radiation.

We summarize the results of the convergence study as well as the error analyses, for both amplitude and phase of the (2,2) mode, in Fig. (4). We show the error from different sources: the PITTNull resolution $err_{\text{PIT}}(N^{-p})$, the extraction radius $err_{\text{PIT}}(R^{-p})$, and the GR-Athena++ resolution $err_{\text{GRA}}(N^{-p})$, where p denotes the convergence order. Additionally, we represent the total error with a solid blue line. This total error is calculated as the quadrature sum of the individual errors.

In Fig. (4), we observe that the PITTNull resolution error for the phase, denoted as $err_{\text{PIT}}(N^{-p})$, is the smallest error among various sources of error for all mass ratios except $q = 1$. For amplitude, $err_{\text{PIT}}(N^{-p})$ is smallest only for mass ratios $q = 3$ and $q = 4$. The phase error shows a slight increase as we approach the merger, ranging from $(10^{-5}, \sim 10^{-3})$ for different mass ratios. In contrast, the error in amplitude remains relatively constant for $q = 2, 3,$ and 4 cases, and it is slightly increasing only for $q = 1$. The range of this error is in $(10^{-4}, \sim 5 \times 10^{-2})$.

The error of the extraction radius is denoted by $err_{\text{PIT}}(R^{-p})$ in Fig. (4). We observe that the largest source of error is due to the extraction radius for both phase and amplitude. To mitigate this error, one can use a larger extraction radius. For example, by using a radius of 100, the error term reduces by a factor of 4, cf. Eq. (7). However, only the strains with the extraction radius of 50 show a consistent convergence order. Moreover, as we discuss in Sec. (III C), the strains with the extraction radius of $R = 50$ exhibit much smaller mismatch than $R = 100$. Consequently, we select to use strains with world tube excretion $R = 50$ for our analysis.

In Fig. (4), we see that the error in the phase and amplitude associated to the GR-Athena++ resolution, $err_{\text{GRA}}(N^{-p})$, is relatively larger during the inspiral for high mass ratio runs compared to lower mass ratio runs with $q = 1$ and 2. Moreover, this error grows as it gets close to the merger, and it is within the range of $(10^{-5}, 10^{-2})$ for both phase and amplitude.

For $q = 2, 3,$ and 4, we observe in Fig. (4) that during the inspiral, and after junk radiation, the total error for the dephasing is less than 0.01 radians. Moreover, the total error for the amplitude relative difference is below $\sim 1\%$. As we get close to the merger, the total error for these cases increases but still remains below 0.05 radians for the phase and below $\sim 5\%$ for the amplitude relative difference. For $q = 1$, we see a larger total error, in its phase and amplitude, with respect to the higher mass ratio runs.

Lastly, we find that the CCE strains derived from $N^{\ell m}$ show no discernible convergence pattern for neither the resolution nor the world tube extraction radius. Consequently, we have opted not to include these results in our analysis.

C. Self-mismatch

Presuming our highest resolution run produces the most accurate waveform, we assess the accuracy of our NR simulations for different extraction radii by comparing the agreement between this waveform and the waveforms generated from simulations with identical initial data but lower resolutions. To quantify this, we use the noise-weighted inner product between two Fourier-domain waveforms, h and h' :

$$(h | h') = 4\mathbb{R} \int_{f_{\text{low}}}^{f_{\text{high}}} df \frac{\tilde{h}^* \tilde{h}'}{S_n(f)}, \quad (9)$$

for a detector noise power spectrum, $S_n(f)$ and compute the overlap \mathcal{O} between the two waveforms [93, 94]:

$$\mathcal{O}(h, h') = \max_{\Delta t_c, \Delta u} \frac{(\hat{h}' | \hat{h}_+)^2 + (\hat{h}' | \hat{h}_\times)^2 - 2(\hat{h}' | \hat{h}_+)(\hat{h}' | \hat{h}_\times)(\hat{h}_+ | \hat{h}_\times)}{1 - (\hat{h}_+ | \hat{h}_\times)^2}. \quad (10)$$

Here, $\hat{h}_{+/\times} = \frac{h_{+/\times}}{\sqrt{(h_{+/\times} | h_{+/\times})}}$ represents the unit-normalized polarization, and

$$u = \frac{F_+ \sqrt{(h_+ | h_+)}}{F_\times \sqrt{(h_\times | h_\times)}}$$

depends on the detector response function $F_{+/\times}$. The maximisation over the peak time difference Δt_c is performed efficiently using an inverse fast Fourier transform routine. Thus, by definition, for a chosen inclination angle ι Eq. (10) is effectively maximized over an overall amplitude scaling, time differences, sky location, and polarization angle. The overlap $\mathcal{O} = 1$ if the two waveforms

are identical up to a re-scaling; otherwise, $\mathcal{O} < 1$. This reduces to:

$$\mathcal{O}(h, h') = \max_{\Delta t_c}(\hat{h}' | \hat{h}_+) \quad (11)$$

when $\hat{h}_+ = i\hat{h}_x$, as is the case when comparing the individual modes (ℓ, m) for each waveform.

It must be noted that Eq. (10) does not account for the two waveforms' phase differences, $\Delta\phi$ that can affect the distinguishability or ‘‘mismatch’’ between the two waveforms. Therefore, for each pair of waveforms, we numerically maximize over $\Delta\phi$ and calculate the mismatch:

$$\mathcal{M}(h, h') = 1 - \max_{\Delta\phi} \mathcal{O}(h, h') \quad (12)$$

which measures the inconsistency between the two NR waveforms. Consistent with the rest of the paper, we use the strains obtained using the CCE method with the world tube extraction radii of 50 and 100.

Our goal is to assess the mismatch of the highest resolution run in table (I) against the ‘exact’ benchmark, i.e., an infinite resolution run, for the next-generation detectors such as LISA [95], the ET [62], and CE [59]. To this aim, we first model the mismatch between lower resolutions with respect to the highest available resolution in table (I) using

$$\mathcal{M}(p, c, \delta x, \delta x_{ref}) = c \left(\delta x^p - \delta x_{ref}^p \right), \quad (13)$$

where p and c are coefficients to be fit using the data, and δx_{ref} is the resolution of the benchmark run, cf. [74, 96],

Using this ansatz, we can then estimate the mismatch between a waveform at a given resolution δx and the exact solution as $\mathcal{M}(c, p, \delta x, \delta x_{ref} = 0)$.

Fig. (5) shows the mismatch of the (2, 2) mode strains obtained using the CCE method for two different world tube extraction radii of 50, the left panel, and 100, the right panel. We employ the LISA noise curve [97] for this comparison and consider a total mass of $10^5 M_\odot$. The discrete data points represent the mismatch between the highest and the other resolutions. Additionally, the corresponding fit, described by Eq. (13) with $\delta x_{ref} \rightarrow 0$, is shown as a dashed line, with different colors indicating each mass ratio. An upside-down triangle on the dashed line indicates the mismatch between the highest resolution and the exact solution, i.e., evaluating Eq. (13) with the fitted values of c and p and setting $\delta x_{ref} = 0$.

It is important to note that LISA can detect signals with SNR as high as 1000, which requires a mismatch of $\lesssim 10^{-7}$. This is because the extremised loudness difference, $(\delta h | \delta h) = (h - h' | h - h')$, between the waveforms h' and h , depends on the signal's SNR as $2\rho^2(1 - \mathcal{M}(h, h'))$. At an SNR of 1000, this difference, $(\delta h | \delta h) \sim 0.2$, remains below the whitened noise variance of 1, indicating any difference between the waveforms will not manifest as a difference in binary parameter measurement.

We see in the left panel of Fig. (5) that the mismatch between the highest resolution run and the second highest resolution run at $R = 50$ is $\sim 5 \times 10^{-9}$ for all mass ratios. Additionally, we observe that for mass ratios $q = 1$, $q = 2$, and $q = 3$, the mismatch of our highest resolution strain against the ‘exact’ strain is $\sim 10^{-12}$, while the $q = 4$ run exhibits a mismatch $\sim 10^{-11}$. The latter mismatches are orders of magnitude more accurate than the $\sim 10^{-7}$ threshold required by LISA.

In the right panel of Fig. (5), we present the mismatch between the waveforms extracted at $R = 100$. The mismatch between the highest resolution strain and the second highest resolution strain is $\sim 3 \times 10^{-5}$ for $q = 1$, 2, and 3 runs, and $\sim 10^{-4}$ for $q = 4$. The mismatch of the highest resolution strain against the ‘exact’ strain, namely, when $\delta x_{ref} \rightarrow 0$ in Eq. (13), is $\sim 10^{-5}$ for mass ratios of 1, 2, and 3, while it is $\sim 10^{-4}$ for the $q = 4$ run. These mismatches are significantly larger than those observed in the left panel and do not meet the mismatch requirement set by LISA.

Lastly, our mismatch results quantitatively remain unchanged for total masses in the range $(10^4, 10^6)M_\odot$.

D. Comparison with SXS waveforms

We now compare our waveforms with equivalent simulations from the SXS catalog [98–100]. In particular, we show the comparison against simulations SXS:BBH:0180, SXS:BBH:184, SXS:BBH:1179 and SXS:BBH:0167. While we report comparisons for these specific cases, we have also compared with a broader set of SXS waveforms, whose initial configurations match our waveforms. These simulations are chosen based on their low initial eccentricity and high resolution, making them suitable for informing waveform models [101]. For each SXS simulation, we employ the second extraction level and the highest resolution available. To compare these waveforms, we first use Eq. (8) to align them, and find $\Delta\phi_{22}$ and Δt . Then, the other modes are aligned by employing the same Δt and appropriately rescaling $\Delta\phi_{22}$:

$$\Delta\phi_{\ell m} = \Delta\phi_{22} \frac{m}{2}. \quad (14)$$

Fig. (7) shows the comparison between the (2, 2) mode of our waveforms and SXS for all mass ratios considered. The visual agreement between the two waveforms is excellent, with the phase differences throughout the whole inspiral up to merger being consistently below 0.1 rad. Similarly, the amplitude of the waveforms is in good agreement, with relative differences typically below 1% and small oscillations observed during the inspiral phase due to some residual eccentricity in the GR-Athena++ simulations.

Fig. (6), instead, shows the comparison between the $q = 2$ GR-Athena++ and SXS simulations for the $(\ell, m) = \{(2, 2), (2, 1), (3, 3), (3, 2), (4, 4), (5, 5)\}$ modes. Similar plots for the other mass ratios are available in

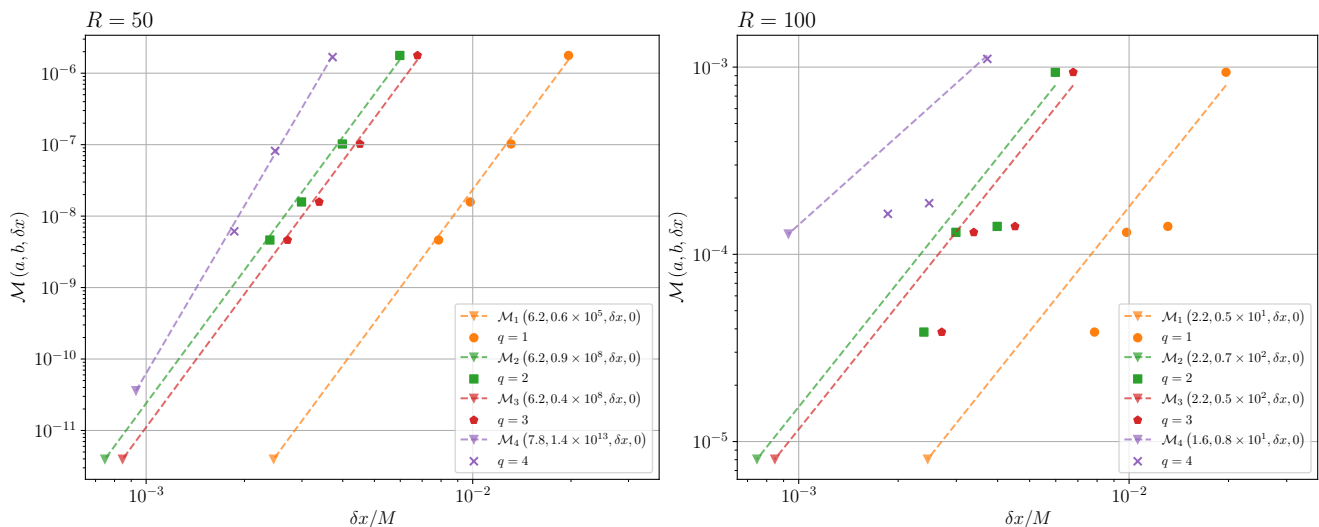


FIG. 5. The discrete points for each mass ratio show the mismatch between low resolution and the highest resolution of CCE strains with (2, 2) mode. The dashed lines estimate the limit of the Eq. (13) at $\delta x_{ref} \rightarrow 0$. The upside-down triangle at the end of each dashed line specifies the mismatch between the highest resolution and the exact resolution. In the left panel we use $C_{klm}(t)$ coefficients extracted at $R = 50$ to compute CCE strains, and in the right panel, the coefficients extracted at $R = 100$.

App. (F). Again, we find good agreement between the two simulations, with the phase differences at merger remaining at the sub-radian level for all modes investigated. The largest discrepancies are observed for the (3, 2) mode, with amplitude relative differences reaching $\sim 20\%$. While it is difficult to ascertain the exact cause of these differences, we note that—as shown in Fig. 9 of Ref. [102]—that the (3, 2) mode is rather sensitive to numerical errors due to the center of mass drift of the binary. This effect is not corrected in the **GR-Athena++** simulations presented here. Additionally, ψ_{32} is affected by large numerical noise, which may also contribute to the observed inconsistencies. Overall, we find that while the dominant quadrupole modes agree to within a few tens of a radian to the SXS waveforms, the computation of precise higher modes is more challenging and may require further investigation, higher resolutions, or improved numerical techniques.

To complement the time-domain comparison, we also quantify the discrepancy between the two waveform catalogs by computing mismatches. We employ the CE and LISA noise curves, and evaluate the mismatches between the starting frequency of the **GR-Athena++** waveform $f_{lm}^0 = m/2\omega_{22}/(2\pi)$ (multiplied by 1.25, to avoid artifacts due to FFTs) and 1024 or 1 Hz, respectively. We compute them between single modes only, as well as for waveform polarizations constructed using the $(\ell, m) = \{(2, 2), (2, 1), (3, 3), (3, 2), (4, 4), (5, 5)\}$ modes, fixing the inclination angle to $\iota = \pi/3$. We use Eq. (12) to compute the mismatches as the output is independent of the sky position of the source. When higher modes are included, we average the obtained mismatches over four values of effective polarization angle u . and four values of reference phase of the target waveform.

Results for single mode mismatches are shown in Fig. (8). When the CE noise curve is employed, mismatches for all modes are always below the 10^{-3} threshold, with the notable exception of the (5, 5) mode for the $q = 3$ case. A clear hierarchy can be observed, with the (2, 2) mode showing the best agreement ($\bar{\mathcal{F}} < 10^{-4}$) for all systems considered, followed by the (4, 4), (3, 3), (2, 1) and (5, 5) modes. When the LISA noise curve is used results are comparable to those previously discussed, although a slight worsening of the agreement is observed at higher masses. Fig. (9), instead, shows the mismatches computed with polarizations constructed using the $(\ell, m) = \{(2, 2), (2, 1), (3, 3), (3, 2), (4, 4), (5, 5)\}$ modes. The initial frequency chosen for the mismatch calculation is $f_0 = 1.25 \times \omega_{22}5/(4\pi)$, to ensure that we are focusing on a frequency region where all modes are present. The mismatches found always lie comfortably below the 10^{-3} threshold for both the CE and LISA noise curves.

These figures indicate that the agreement between the two codes is sufficient for the purposes of current generation observations, and comparable to or better than the accuracy of current state-of-the-art waveform models ($\bar{\mathcal{F}} \sim 10^{-4} - 10^{-3}$). However, with next generation detectors in mind, further improvements—especially in the computation of higher modes—may be necessary.

IV. CONCLUSION AND DISCUSSION

Using the **GR-Athena++** code, we simulated a set of non-spinning BBH systems with mass ratios of 1, 2, 3, and 4, thereby creating the first **GR-Athena++** catalog. We compute CCE strains at null infinity

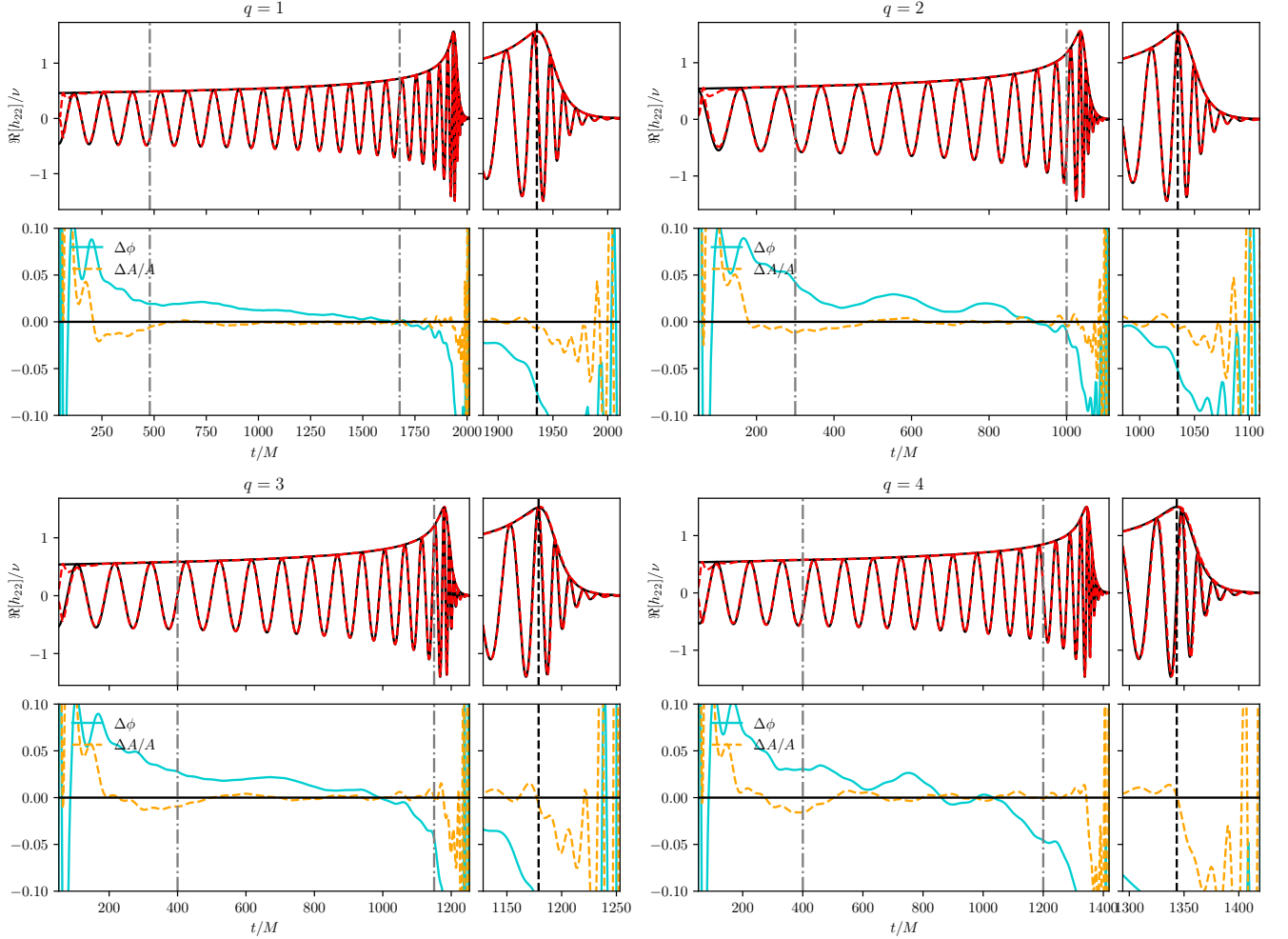


FIG. 6. Comparison of the h_{22} mode between the GR-Athena++ (red dashed) and SXS (black) simulations for all four mass ratios considered. Top panels show the real part of the waveform multipoles, while the bottom panels display the phase difference $\Delta\phi = \phi_{\ell m}^{\text{SXS}} - \phi_{\ell m}^{\text{GRA}}$ and the amplitude relative difference $\Delta A/A = 1 - A_{\ell m}^{\text{GRA}}/A_{\ell m}^{\text{SXS}}$. The vertical dashed-dotted lines indicate the interval used for the alignment, while the vertical dashed lines mark the merger time. We find that phase differences at merger and during the inspiral rarely exceed ~ 0.1 rad, with the $q = 4$ case being the only exception, and amplitude relative differences typically below 1%.

\mathcal{I}_+ using the PITTNull code. Additionally, we study their phase and amplitude convergence with respect to PITTNull’s resolution, the world tube extraction radius, and GR-Athena++’s resolution. We find that the phase evolution shows a clean second-order convergence with respect to PITTNull’s resolution as well as the world tube extraction radius—for the dominant $(2, 2)$ mode. Moreover, the amplitude of CCE strains for the $q = 2, 3$, and 4 runs shows at least a second-order convergence for both PITTNull’s resolution and the world tube extraction radius, but for $q = 1$, it exhibits a first-order convergence with respect to PITTNull’s resolution and no convergence with respect to the world tube extraction radius. Regarding the phase convergence with respect to GR-Athena++’s resolution, $q = 1$ and $q = 2$ BBH runs demonstrate fourth-order and second-order convergence,

respectively; however, the $q = 3$ and $q = 4$ run do not show any convergence in this test. Similarly, the amplitude for $q = 1$ and $q = 2$ cases shows fourth-order convergence and no convergence for $q = 3$ and $q = 4$ runs.

Accounting for all sources of error from PITTNull and GR-Athena++ codes, we find that for the $q = 1$ binary, the phase uncertainty is of the order of 10^{-2} radians during the inspiral and peaks at ~ 0.1 radians at merger. The amplitude error similarly grows from 1% during the inspiral to up to 10% at merger. In either cases, the uncertainty is dominated by the extrapolation of the waveforms to \mathcal{I}_+ using PITTNull. The error budget for phase and amplitudes for the other binaries is about a factor two smaller and, for $q = 2$ and $q = 3$, is also dominated by CCE. The $q = 4$ runs, are the only one for which the

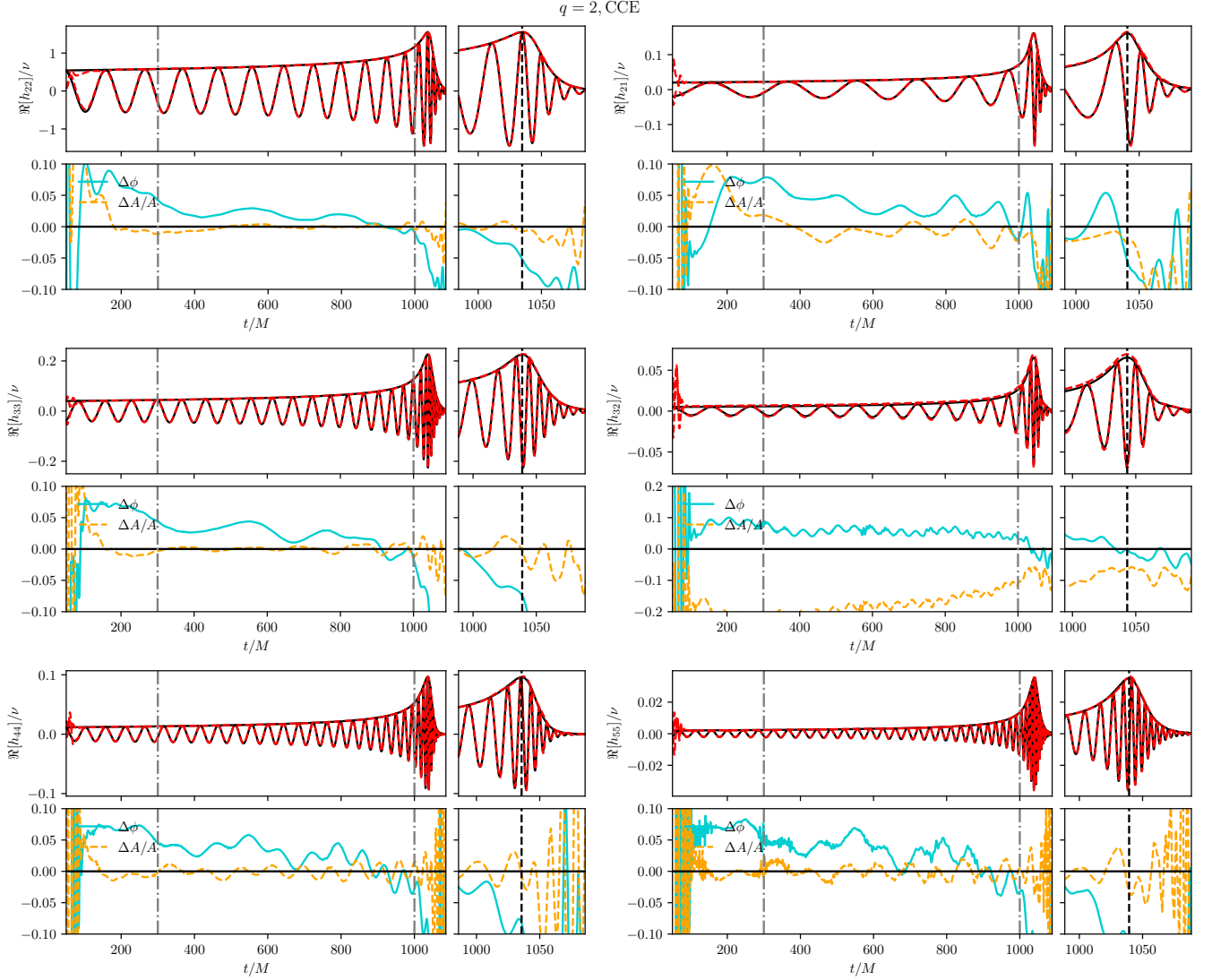


FIG. 7. Comparison of **GR-Athena++** (red dashed) and SXS (black) waveforms for the $(\ell, m) = \{(2, 2), (2, 1), (3, 3), (3, 2), (4, 4), (5, 5)\}$ modes and $q = 2$. Top panels show the real part of the waveform multipoles, while the bottom panels display the phase difference $\Delta\phi = \phi_{\ell m}^{\text{SXS}} - \phi_{\ell m}^{\text{GRA}}$ and the amplitude relative difference $\Delta A = 1 - A_{\ell m}^{\text{GRA}}/A_{\ell m}^{\text{SXS}}$. The vertical dashed-dotted lines indicate the interval used for the alignment of the $(2, 2)$ mode, while the vertical dashed lines mark the merger time. We find overall excellent agreement between the two waveforms, with phase differences at merger and during the inspiral rarely exceeding ~ 0.1 rad. The largest differences are observed for the $(3, 2)$ merger-ringdown portion. See the text for further details.

finite-resolution error is comparable — although smaller than the CCE error.

Had we accounted only for finite-resolution uncertainties in the **GR-Athena++** simulations, we would have concluded that, for mass ratios of 1, 2, 3, and 4, the waveforms are sufficiently accurate for application in next-generation detectors such as LISA, where SNR can be as high as 1000. Unfortunately, the differences between waveforms at \mathcal{I}_+ obtained by running **PITTNu11** for different inner radii are substantial. This is an unexpected finding, which indicates that even though the intrinsic error in the **GR-Athena++** simulations is very small, the

overall quality of our waveform is somewhat compromised. These are nevertheless among the most accurate puncture-based waveforms for BBH to date.

We compared our results with those from the SXS catalog and confirmed that our waveforms are in agreement with those produced by the SXS collaboration, with typical phase differences below 0.1 radians throughout the inspiral and merger phases and *maximum* mismatches of the order of 10^{-3} for both the CE and LISA noise curves. These numbers indicate that our waveforms are in good agreement with those produced by the SXS collaboration for the considered number of cycles. This valida-

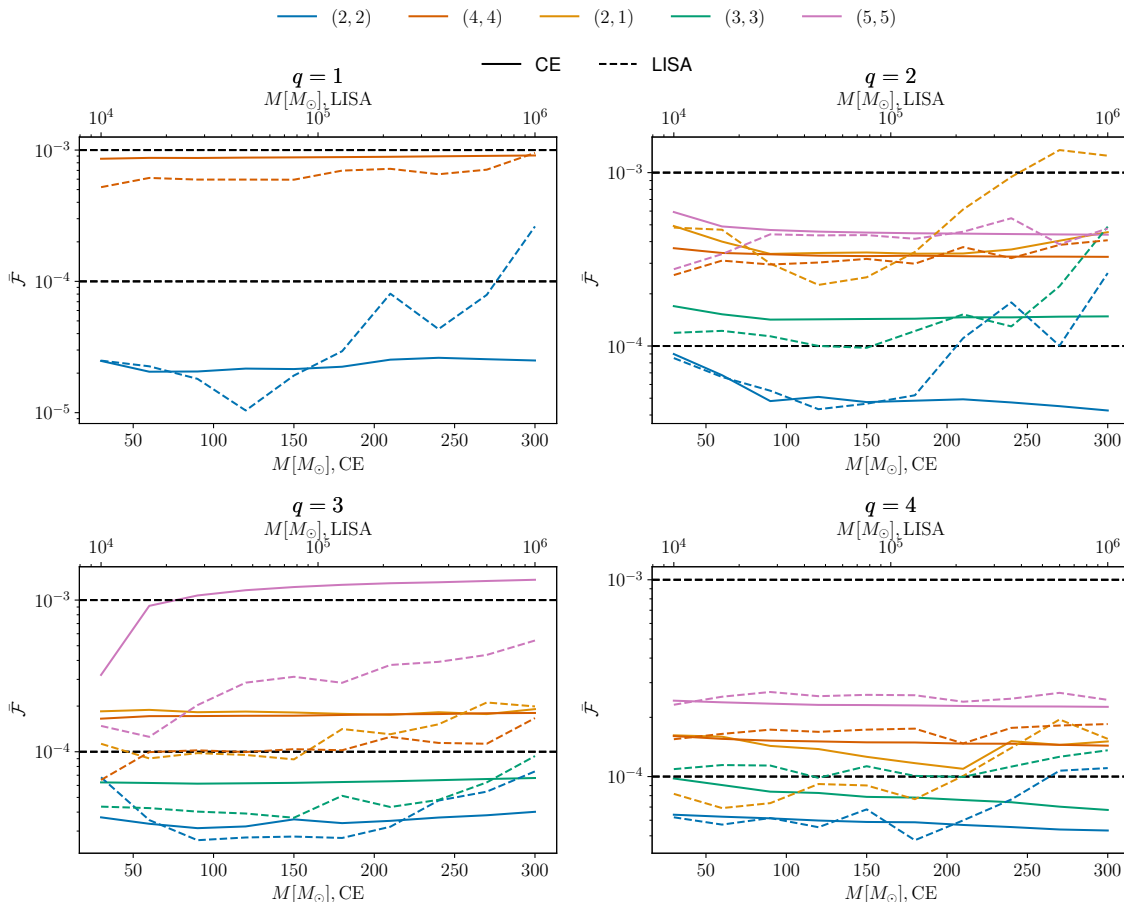


FIG. 8. Single-mode mismatch between **GR-Athena++** and SXS waveforms for the (2, 2), (2, 1), (3, 3), (4, 4), (5, 5) modes obtained with the CE (straight lines) and LISA (dashed lines) noise curves at varying mass ratios. In both cases mismatches typically lie below the 10^{-3} threshold, with the only exception being the (5, 5) mode for $q = 3$ and the (2, 1) mode for $q = 2$. Overall, the agreement between the two codes is of accuracy comparable to (or better than) current NR-informed waveform models.

tion process is essential for establishing the credibility of our results and ensuring that they align with existing data from other established sources. Our work also provides another independent confirmation of the accuracy of the SXS waveform catalog, which is widely used for GW waveform modeling and data analysis applications. That said, the differences between our waveforms and those from the SXS collaboration are significantly larger than the uncertainties we have estimated for our data. These inconsistencies could be the result of gauge or initial data differences, or due to some other, unidentified source of systematic uncertainty in our waveforms or in the SXS catalog. Additional work, carefully cross validating **GR-Athena++** with SXS’s **SpEC** [20] and **SpECTRE** [20] codes, is needed to understand the origin of these discrepancies.

Our work demonstrate that finite-differencing moving-puncture methods can produce highly accurate BBH simulations, with quality comparable to those obtained with spectral methods. On the other hand, we have identified

a new source of systematic uncertainties in NR data in the commonly adopted method to extrapolate waveforms to future null-infinity via CCE. This dominates the error budget for our waveforms. Future work will be dedicated to address this source of error, in particular, we plan to interface **GR-Athena++** with the publicly available CCE in **SpECTRE** [103]. We also plan to extend the **GR-Athena++** catalog with the inclusion of higher mass ratios, eccentric, and spinning BBH configurations. Finally, additional work is needed to understand the discrepancies between our results and those of the SXS catalog, starting with a more detailed investigation of the effect of eccentricity in the **GR-Athena++** simulations and the impact of the center of mass drift.

ACKNOWLEDGMENTS

The authors would like to thank A. Nagar and S. Albanesi for valuable discussions throughout the develop-

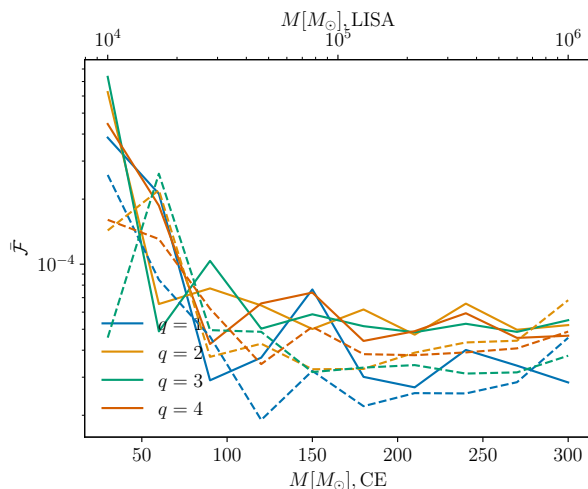


FIG. 9. Mismatch between GR-Athena++ and SXS waveforms computed using polarizations constructed from the (2, 2), (2, 1), (3, 3), (3, 2), (4, 4), (5, 5) modes. The mismatches are averaged over four values of effective polarization angle and four values of reference phase of the target waveform. The agreement between the two codes is of accuracy comparable to or higher than current NR-informed waveform models for both the CE (straight lines) and LISA (dashed lines) noise curves, and always below the 10^{-3} threshold.

ment of this project. This work was supported by NASA under Award No. 80NSSC21K1720. RG acknowledges support from NSF Grant PHY-2020275 (Network for Neutrinos, Nuclear Astrophysics, and Symmetries (N3AS)). KC acknowledge the support through NSF grant numbers PHY-2207638, AST-2307147, PHY-2308886, and PHY-2309064. SB and BD knowledge support by the EU Horizon under ERC Consolidator Grant, no. InspiReM-101043372.

Simulations were performed on Frontera (NSF LRAC allocation PHY23001), and on the national HPE Apollo Hawk at the High Performance Computing Center Stuttgart (HLRS). The authors acknowledge HLRS for funding this project by providing access to the supercomputer HPE Apollo Hawk under the grant number INTRHYGUE/44215 and MAGNETIST/44288.

Appendix A: Finite radius extraction method

In the FRE method, the $\psi_4^{\ell m}$ modes are extracted at a specific radius R to construct the Newman-Penrose scalar Ψ_4 as follows [11, 104]:

$$\Psi_4 = \sum_{\ell=2}^{\infty} \sum_{m=-\ell}^{\ell} \psi_4^{\ell m}(t) {}_{-2}Y^{\ell m}(\vartheta, \varphi), \quad (\text{A1})$$

in which ${}_{-2}Y^{\ell m}(\vartheta, \varphi)$ is the spin-2 weighted spherical harmonic. Ψ_4 is also related to h_+ and h_\times via Eq. (3).

To obtain GW strains at null infinity, we first use the following formula to construct $\psi_4^{\ell m}$ at null infinity [105,

106]

$$\lim_{r \rightarrow \infty} r \psi_4^{\ell m} \simeq A \left(\bar{r} \psi_4^{\ell m} - \frac{(\ell-1)(\ell+2)}{2\bar{r}} \int dt \bar{r} \psi_4^{\ell m} \right) + \mathcal{O}(R^{-2}) \quad (\text{A2})$$

where $A = 1 - 2M/\bar{r}$ and $\bar{r} = R(1 + M/(2R))^2$. We then use either a time domain integration or an FFI method (see App. (B)) to obtain GW strains at null infinity.

Appendix B: Fixed frequency integration

The time domain integration method is error prone, involving the subtraction of various polynomials during each time integration step, which can potentially impact the waveform content. To avoid this, we use the FFI method [87].

During the FFI process, preserving the waveform's physical frequency range is essential. To achieve this, the following cutoff frequency:

$$f^{\text{cutoff}}(m) = \frac{\Omega_{\text{orb}}}{3\pi} \max(1, m), \quad (\text{B1})$$

is used for each m mode. Here, Ω_{orb} is the orbital angular velocity calculated using the Newtonian approximation $\Omega_{\text{orb}} = \frac{(q+1)^2}{qD} P_y$.

Finally, it is worth mentioning that to compute the second term of Eq. (A2) we use FFI. Time-domain integration introduces nonphysical modulations in strain amplitude, and post-merger waveforms do not converge to zero as seen in Fig. (10).

Appendix C: FRE convergence

This section quantifies the numerical errors in the GW strain obtained using the FRE method due to resolution and radius extraction at null infinity. We use the same procedure outlined in Sec. III B, and the results of the convergence analysis for the phase is shown in Fig. (11)

We extract the waveforms at $R = 100$ and employ three distinct resolutions from the table (I). Each row in Fig. (11) corresponds to a specific mass ratio, while each column corresponds to a specific mode. Focusing on the dominant (2, 2) and (4, 4) modes, we use the method described in Sec. (II E), and we find convergence behavior in all cases.

Similarly, we choose the highest resolution and perform the analysis for different extraction radii to determine the convergence order for the phase and amplitude of the FRE strains. The outcomes of this analysis are illustrated in Fig. (12). Across all cases, except $q = 2$,

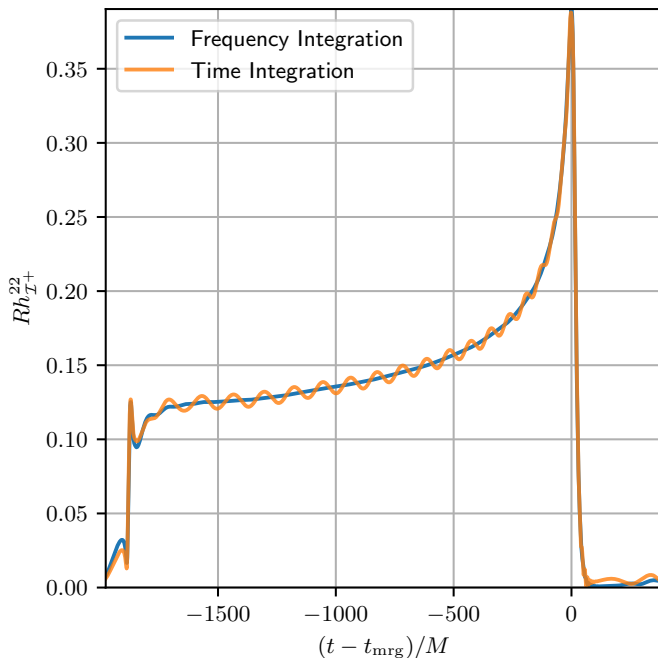


FIG. 10. Strains at null infinity (\mathcal{I}^+) for the $q = 1$ system. We use two different integration methods to compute $r\psi_4^{22}$ at \mathcal{I}^+ , namely FFI (blue) and time domain integration (orange). Given $r\psi_4^{22}$ at \mathcal{I}^+ , we use FFI to calculate the strains. We observe that time domain integration gives rise to nonphysical modulations in the middle of the strain and values larger than the frequency integration in the tail.

we observe that strains converge with respect to the extraction radius².

After determining the convergence order, we quantify the leading order error term for the highest available resolution waveform with $R = 100$. To assess the resolution error, we align this waveform with the second-highest resolution one using Eq. (8) and apply equation Eq. (7). Similarly, we use the highest resolution waveform extracted at radius 100 and 80 for the extraction radius error, and then employ equation Eq. (7).

Fig. (13) summarizes the error analysis results. The term $err(N^{-p})$ represents the error associated to resolution of GR-Athena++, while $err(R^{-p})$ denotes the error arising from the extraction radius. Here, p indicates the order of convergence found in each convergence study. We observe that the dominant error arises from the extraction radius, and the total error increases as we approach the merger. The largest errors are observed for the $q = 1$ case, where the total error reaches ~ 0.1 radians, and the relative amplitude difference becomes $\sim 10\%$. Higher mass ratio runs show smaller errors, with $q = 2$ approaching $\Delta A/A \sim 5\%$ and $\Delta\phi \sim 0.01$ radians. For

the $q = 3$ and 4 systems, the maximum total error is ~ 0.05 radians in phase, and $\sim 5\%$ in the relative amplitude difference.

Appendix D: FRE vs CCE

We investigate the discrepancies between the (2,2) modes of the CCE and FRE strains for our simulations. The left column of Fig. (14) compares the phase difference $|\Delta\phi|$ between the highest available resolution of GR-Athena++ (FRE strain with radius 100), and PITTNull (CCE strain with radius 50). Similarly, in the right column, we compare the amplitude between the FRE and CCE strains using $|\Delta A/\bar{A}| := |(A_{\text{CCE}} - A_{\text{FRE}})/\bar{A}|$, where $\bar{A} = (A_{\text{CCE}} + A_{\text{FRE}})/2$. The difference between the two methods, i.e., $\Delta\phi$ and $|\Delta A/\bar{A}|$, is shown by a black solid line. We observe that $\Delta\phi$ increases while $|\Delta A/\bar{A}|$ decreases as we approach merger. The maximum $\Delta\phi$ is ~ 0.1 radians and is found for the $q = 4$ run, and occurs at the merger; however, the other mass ratio runs have slightly smaller errors compared to $q = 4$. Lastly, $|\Delta A/\bar{A}|$, among all runs, barely reaches 3% relative difference, cf. [107].

Using numerical error estimates for the phase, obtained in Sec. III B and Sec. C, we plot the total numerical error $err = |err_{\text{CCE}}| + |err_{\text{FRE}}|$ in Fig. (14). We see that in $q = 1$ and 3 case, the total numerical error is bigger than or comparable with $\Delta\phi$, and hence, we can expect that the difference in phases of the FRE and CCE strains are due to the numerical errors contained within each code, i.e., GR-Athena++ and PITTNull. However, for $q = 2$ and 4, we observe dephasing is greater than the numerical error, therefore, it suggests that we are underestimating the error for one or both waveforms.

Similarly, we use the numerical errors of GR-Athena++ and PITTNull codes for amplitude found in Sec. III B and Sec. C, to compute the total numerical error by $err = (|err_{\text{CCE}}A_{\text{CCE}}| + |err_{\text{FRE}}A_{\text{FRE}}|)/\bar{A}$. For the amplitude comparison, we see that total numerical error is greater than or comparable to $|\Delta A/\bar{A}|$. As such, it indicates that the observed deviation between the FRE and CCE amplitudes falls within the numerical error region, suggesting that the differences between the two methods can be attributed to the expected numerical errors in the codes.

Lastly, when we compare the numerical errors of err_{CCE} and err_{FRE} , we see that after the junk radiation err_{CCE} is always the smaller one, in all cases.

Appendix E: Fourier filtering in CCE

At the beginning of the evolution, and sometimes even at later stages, C_{klm} in Eq. (1) exhibits noise. This noise, often stemming from numerical errors, manifests as high-frequency signals with small amplitudes, as depicted in Fig. (15). In an effort to mitigate these errors, Ref. [16]

² While for $q = 2$ run we see no convergence in phase with respect to the extraction radii, we observe a 2nd order convergence in amplitude.

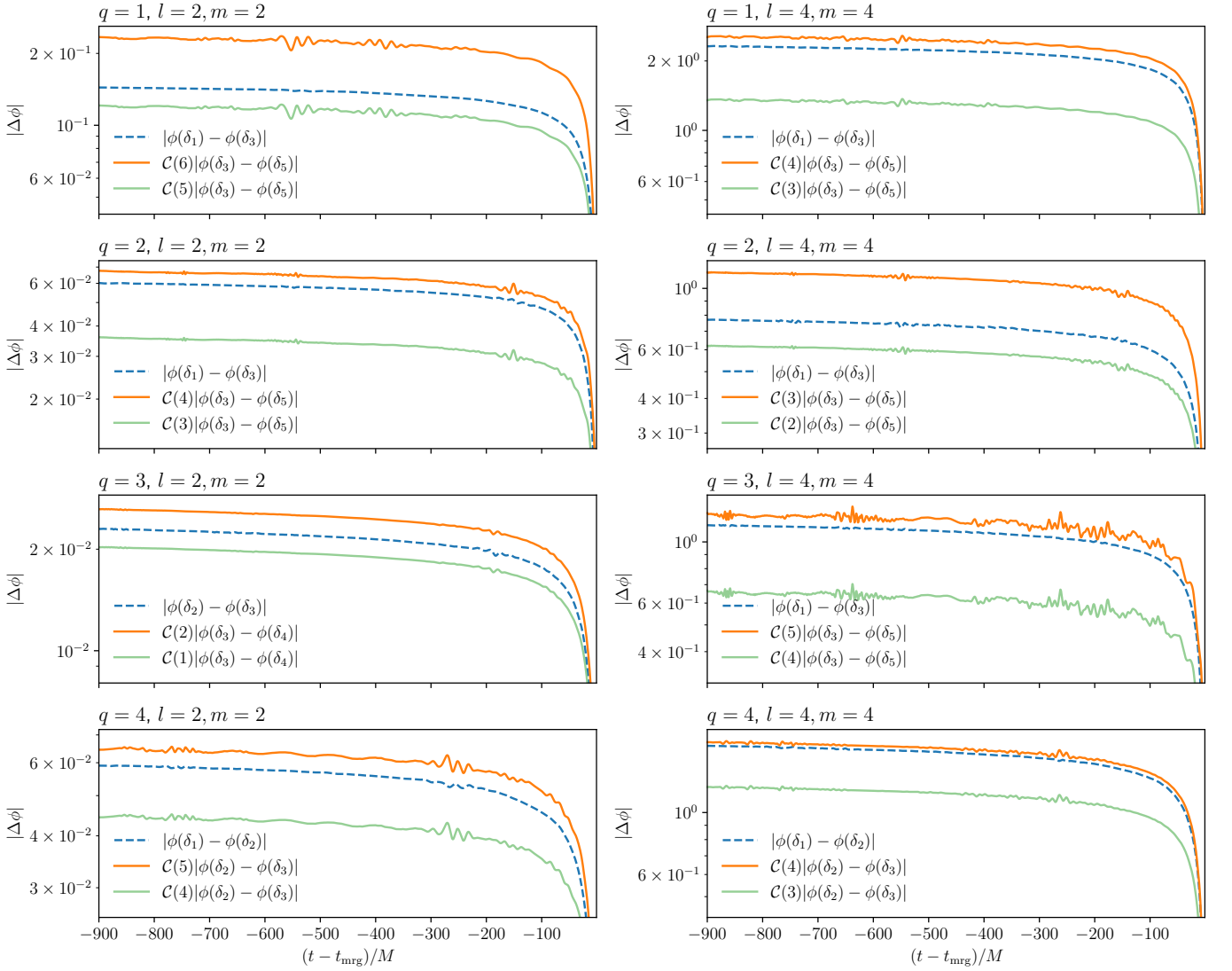


FIG. 11. Convergence study of strains using the FRE method. Here, $\delta_i^{-1} \in \{128, 192, 256, 320, 384\}$, for $i = 1, 2, 3, 4, 5$. We extrapolate $\psi_4^{\ell m}$ to null infinity using Eq. (A2). The pertinent strain is computed via FFI. Left column shows $l = 2, m = 2$ mode and right column shows $l = 4, m = 4$ mode for different mass ratios. The location of dashed line with respect to colored solid lines indicates the order of convergence.

drops the high frequency content of the signal. In particular, Ref. [16] employs a Fourier transformation of the signal $h(t)$ to obtain the signal in Fourier space, $\tilde{h}(k)$, where $k = \frac{\omega T}{2\pi}$, T is the total time, $\omega = \frac{d\phi(t)}{dt}$, and $\phi(t)$ is $\psi_4^{\ell m}$ phase. Then, they truncate the high-frequency noises by multiplying $\tilde{h}(k)$ with

$$\frac{1}{2} (1 - \text{erf}(-(k - k_{\max}))), \quad k_{\max} = \frac{\omega_{\max} T}{2\pi}, \quad (\text{E1})$$

in which ω_{\max} is the maximum of $\frac{d\phi(t)}{dt}$. Subsequently, through an inverse transformation, they obtain a refined strain in time.

Since Fourier transformation assumes periodicity of the wave, a challenge is encountered when the wave is not periodic. To enforce periodicity, one might be inclined to

apply windowing techniques at both ends of the data. But, it is crucial to recognize that the data pertains to metrics (through C_{klm}) rather than $\psi_4^{\ell m}$. As such, applying windowing on the data is prone to introducing non-physical values for the metric. To address this periodicity requirement, Ref. [16] subtracts a second-order polynomial from both ends of the signal, thereby imposing periodicity. Following the removal of higher frequencies, the previously subtracted polynomial is reintroduced to yield the filtered data.

The comparison presented in Fig. (15) illustrates the efficacy of the filtering methodology proposed by [16]. When compared with the unfiltered data, this Fourier-based filtering technique demonstrates the capacity to attenuate a portion of the high-frequency noise.

Nevertheless, the presence of imperfect periodicity at

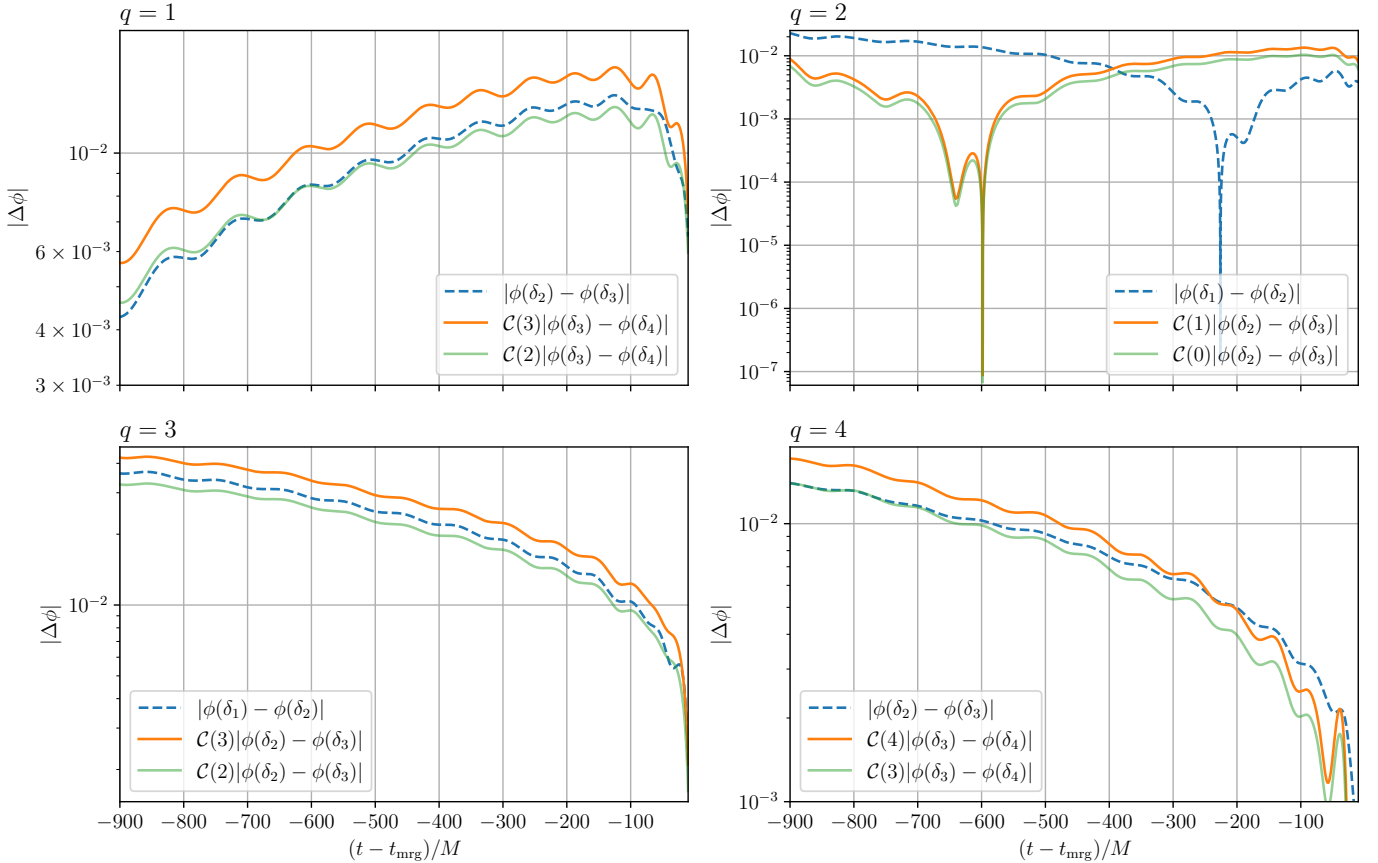


FIG. 12. Radius convergence of the FRE (2,2) mode for different mass ratios. Here, $\delta_i^{-1} \in [60, 80, 100, 120]$. We observe convergence for all mass ratios, except for the $q = 2$ case.

the edges of the dataset introduces spectral leakage, impeding a rapid decay of Fourier coefficients. Consequently, when using the PITTNull code to analyze $\psi_4^{\ell m}$ and $N_4^{\ell m}$, oscillatory patterns become apparent, particularly at the boundaries of the data.

To assess the impact of noise present in the coefficients, we compare the FRE and CCE $\psi_4^{\ell m}$. The comparison is illustrated in Fig. (16). The results indicate that the FRE method yields smoother data. Nevertheless, as shown in App. (D), the FRE strains exhibit larger uncertainties compared to the CCE strains.

In an effort to enhance the filtering method further, a strategy is devised to enforce perfect periodicity on the data without introducing any nonphysical data points. This is achieved by smoothly extending the data from both ends using an odd reflection technique. Essentially, an odd transformation is applied with respect to each endpoint of the waveform to extend it symmetrically. Subsequently, a window function is used to nullify the waveform values in the artificially extended regions. Following this step, the extended data undergoes truncation to retain only the physically meaningful portion.

It is important to acknowledge that as a result of extending the data and applying filtering, the tails of the data exhibit some wave patterns. Despite the enhance-

ments made to the Fourier filtering technique, resulting in smoother $\psi_4^{\ell m}$ and $N_4^{\ell m}$ data, residual noise still persists. The comparison presented in Fig. (17) highlights the amplitude disparities between the original filtered data, the improved filtered data, and the unfiltered dataset.

The original filtering process of Ref. [16] which applied on signals that are not perfectly periodic, while marginally smoothing the C_{klm} data, introduces pronounced oscillations after using the filtered C_{klm} in the PITTNull code, particularly at the waveform tails, and hence it introduces additional noise compared to the original unfiltered data. As such, the original filter is less favorable for filtering purposes. Conversely, the improved “New” filter, which imposes perfect periodicity, demonstrates a reduction in noise levels compared to the original data. However, due to the imposition of periodicity, the improved filtering method introduces minor oscillations only at the waveform tails.

Although the improved filtering method shows effectiveness in reducing noise at the initial stages of the simulations, however it may introduce modulations at later times.

Given the challenges encountered with filtering methods, including data alterations and waveform noises’ persistence, the decision is made to forego filtering alto-

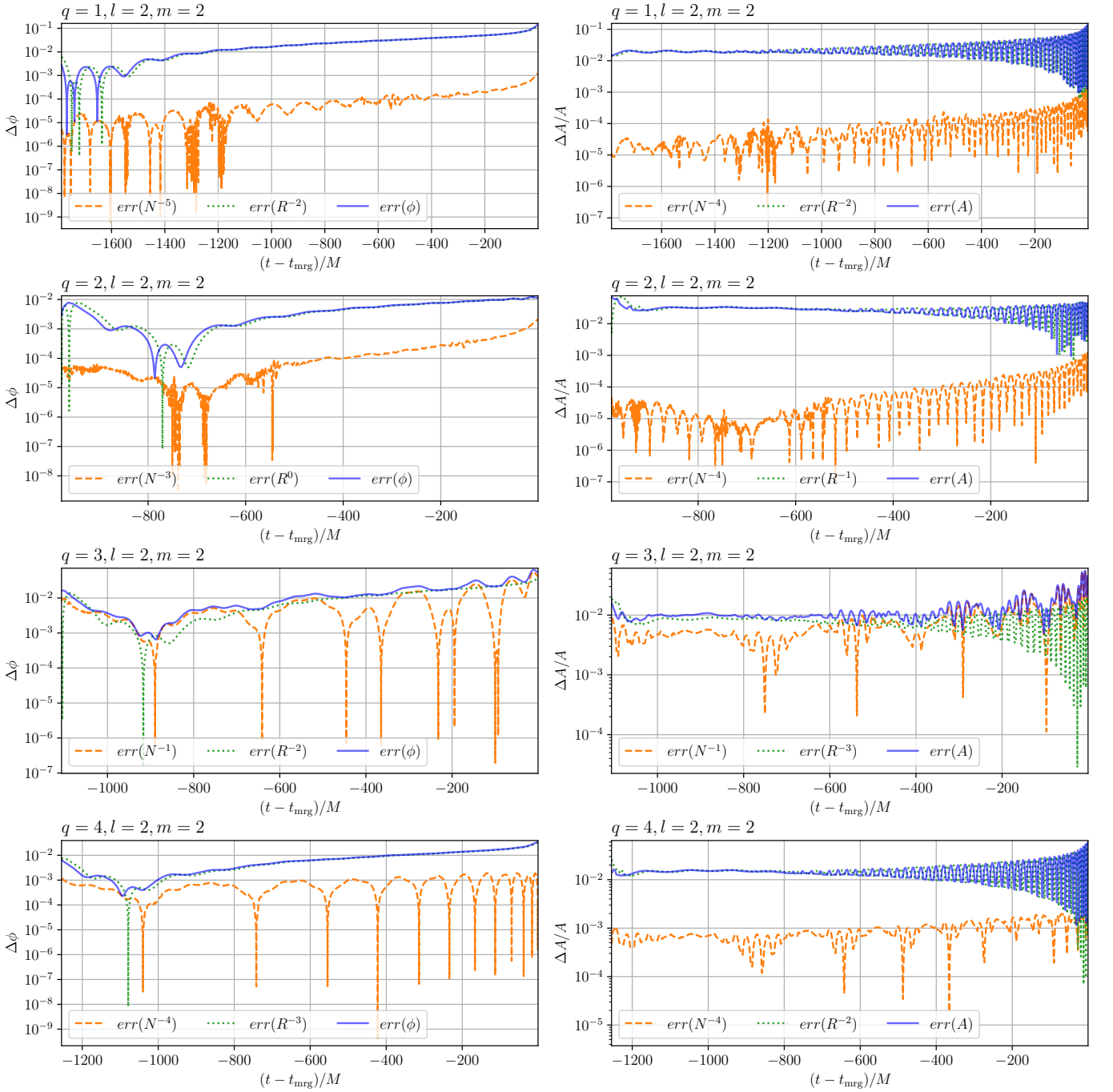


FIG. 13. Sum of errors in the FRE strains for the (2,2) mode. $err(N^{-p})$ denotes the error of the highest resolution run with the extraction radius of 100 in the table (I). p indicates the convergence order. Similarly, $err(R^{-p})$ represents the error for the radius 100, where to find the error we use radii 80 and 100 in Eq. (7). The total error err for ϕ as well as the relative amplitude $\Delta A/A$ is computed by $err = (err^2(N^{-p}) + err^2(R^{-p}))^{1/2}$.

gether. Additionally, using the FFI method on $\psi_4^{\ell m}$ to obtain strains implies filtering large frequency noises that appear in $\psi_4^{\ell m}$. As we observe in Fig. (2), the resultant strains are mostly free of noises.

With filtering not used, the focus shifts to determining the most suitable extraction radius for obtaining the boundary condition for the PITTNull code. This choice

becomes pivotal in ensuring the accuracy and reliability of the data extraction process.

In order to evaluate the impact of the boundary condition world tube radius on waveforms, Fig. (18) presents the amplitude of $\psi_4^{\ell m}$ obtained using CCE for various radii. Upon examining the waveform at its onset, it becomes apparent that smaller extraction radii yield

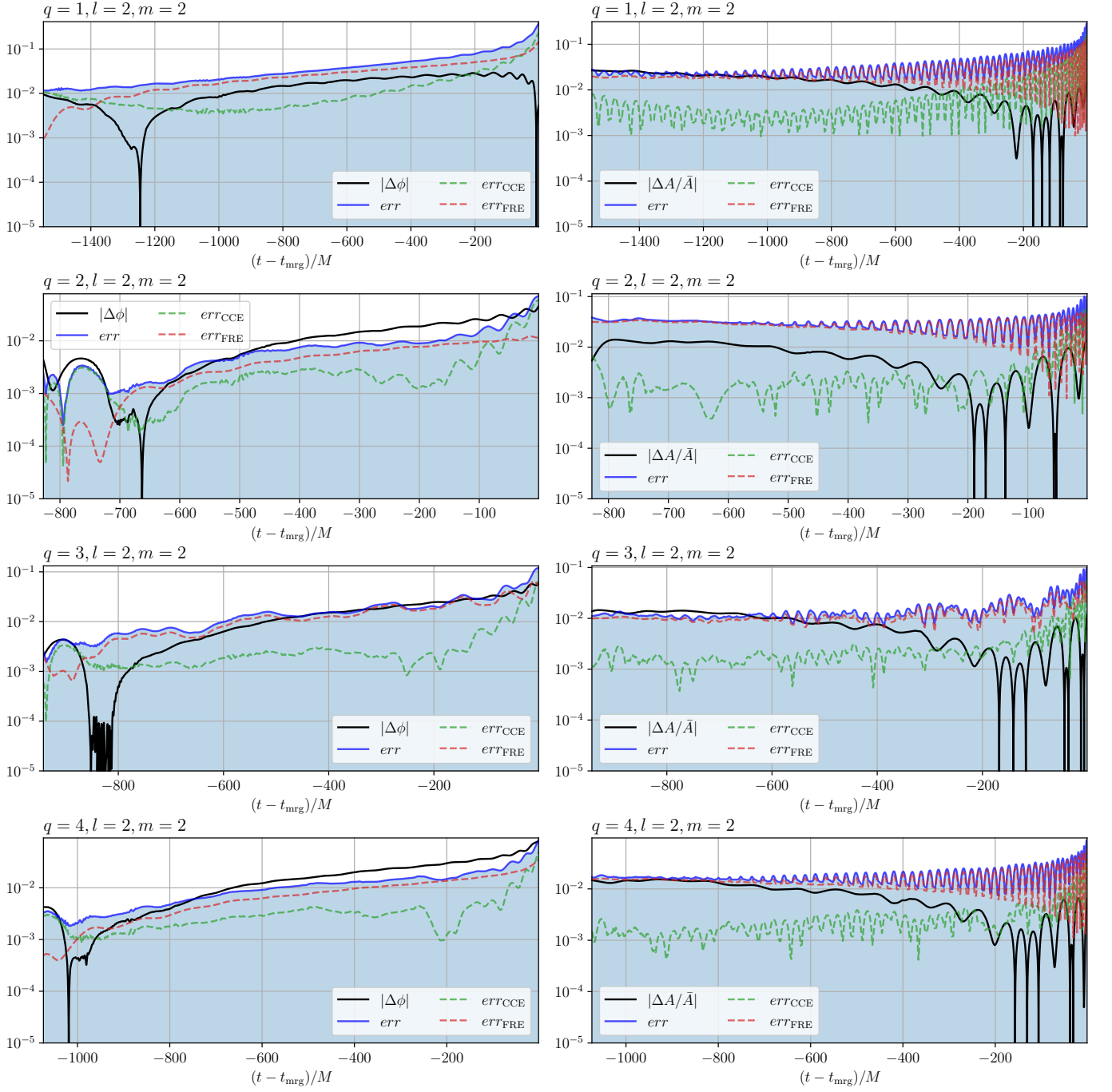


FIG. 14. Difference between FRE and CCE strains. Left columns show the difference between the phase of FRE and CCE strains, $|\Delta\phi| = |\phi_{\text{CCE}} - \phi_{\text{FRE}}|$ — marked by black solid lines. Right columns show the relative difference between the amplitudes (the solid black line), i.e., $|\Delta A/\bar{A}| := |(A_{\text{CCE}} - A_{\text{FRE}})/\bar{A}|$, where $\bar{A} = (A_{\text{CCE}} + A_{\text{FRE}})/2$. Each row illustrates these comparisons for different mass ratio with the highest available resolution from table (I). The numerical errors for the PITNull code (err_{CCE}), and the GR-Athena++ code (err_{FRE}) are illustrated by dashed lines. The total numerical error is marked by a blue solid line in each panel as well as shaded under its curve for a better visualization. We compute the total numerical error in dephasing by using $err = |err_{\text{PIT}}| + |err_{\text{GRA}}|$, and for the amplitude relative difference by $err = (|err_{\text{CCE}}A_{\text{CCE}}| + |err_{\text{FRE}}A_{\text{FRE}}|)/\bar{A}$.

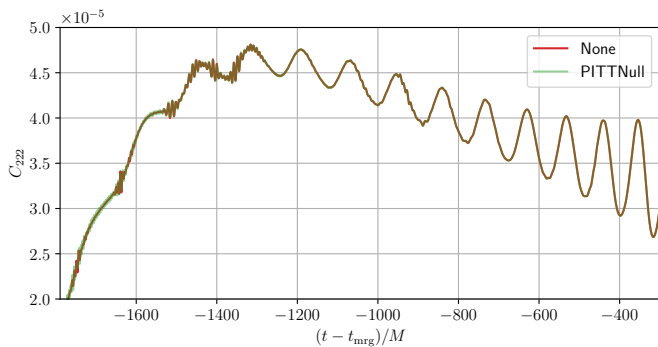


FIG. 15. The coefficient amplitude of C_{222} is plotted for the spatial metric field g_{xx} . The dashed line is the original “None” filtered data, while the solid line, `PITNull`, is the filtered data. The coefficient does not show smooth change from one time step to the next at the beginning of the evolution. In an effort to damp the noises, [16] drops high frequencies of C_{klm} using Eq. (E1).

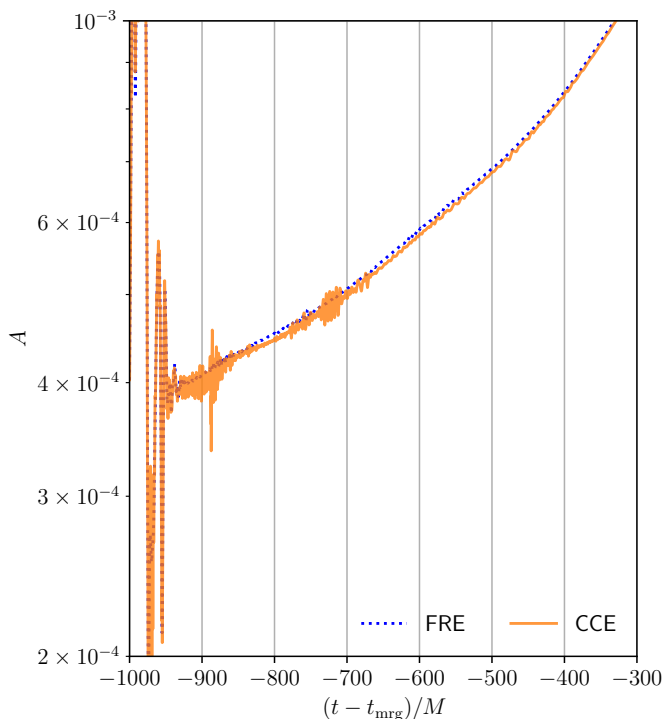


FIG. 16. The FRE method versus the CCE method. The FRE method seems smooth while CCE exhibits oscillations, specially at the beginning of the run.

smoother results with reduced noise levels. However, it is important to note that although the smallest radius may offer smoother results, we do not observe a clean convergence with respect to the `PITNull` resolutions. Consequently, the smallest radius that demonstrates convergence with respect to the `PITNull` resolutions, namely, $R = 50$, see Sec. (III B), is selected for the purposes of this study.

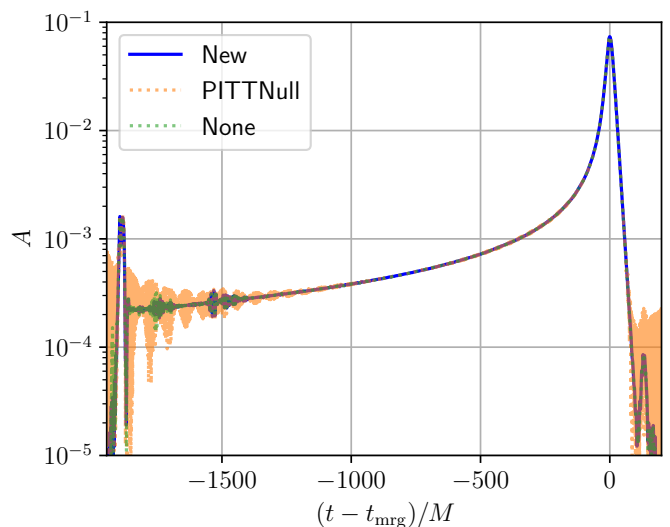


FIG. 17. Comparison of ψ_4^{22} amplitudes, for $q = 1$ BBH system, between original `PITNull` filter developed in [16] and the “New” filter developed in this work, as well as no filtering (“None”). The `PITNull` filter shows strong oscillations at the tails due to non-perfect periodicity. The New filter displays slight oscillation at the tails due to imposing extended periodicity; the amplitude of these oscillations are smaller than the `PITNull` filter. Comparing the `PITNull` filter with the “None” filter, the `PITNull` filter amplifies the noises at early times while the “New” filter damps the noises.

Appendix F: Time domain comparisons with SXS

In this appendix we report time domain comparisons similar to the one presented in the main text (Fig. 6) for all mass ratios considered in this work. The results are shown in Figs. 19, 20 and 21. Quantitative figures such as amplitude and phase differences are comparable with the ones discussed in the main portion of the text for the $q = 2$ system. Phase differences at merger typically remain below a few portions of a radian, with the notable exception of the (3, 2) modes. Notably, this fact remains true also for the $q = 4$ simulation, which was run at a lower resolution with respect to the other systems.

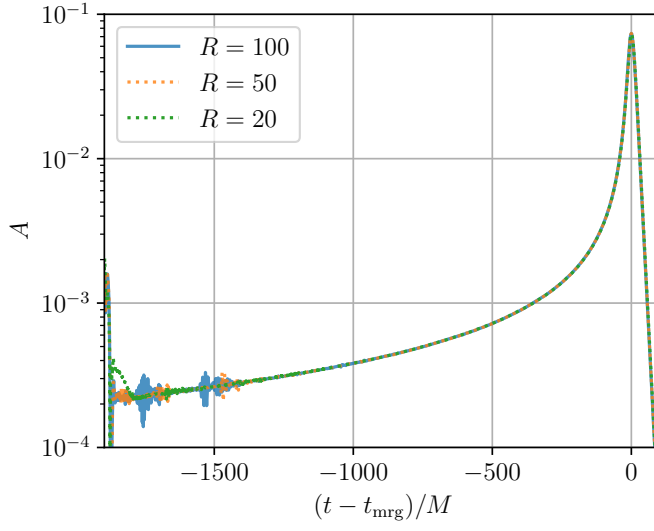


FIG. 18. The amplitude of ψ_4^{22} for various boundary condition extraction radii. While at later time of simulation there is no observable difference between ψ_4^{22} amplitudes, using smaller radii boundary condition extraction for the PITTNull code exhibit less noise at the earlier time of simulation.

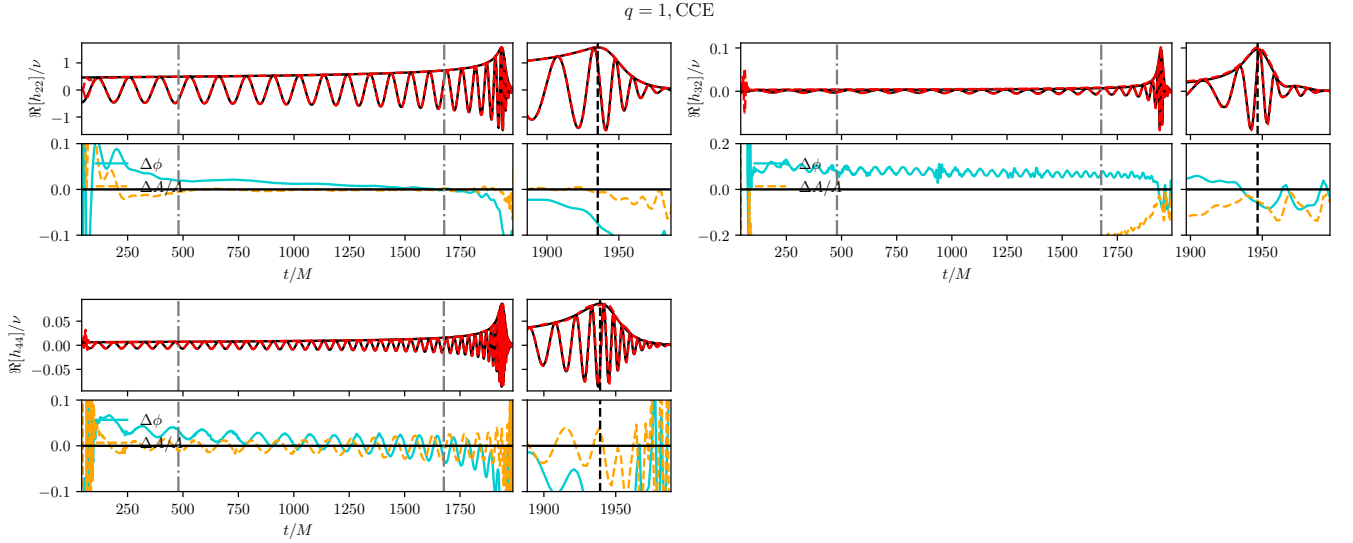


FIG. 19. Time domain comparison between the **GR-Athena++** (red dashed) and **SXS** (black) waveforms for the $(\ell, m) = \{(2, 2), (3, 2), (4, 4)\}$ modes and $q = 1$. Top panels show the real part of the waveform multipoles, while the bottom panels display the phase difference $\Delta\phi = \phi_{\ell m}^{\text{SXS}} - \phi_{\ell m}^{\text{GRA}}$ and the amplitude relative difference $\Delta A/A = 1 - A_{\ell m}^{\text{GRA}}/A_{\ell m}^{\text{SXS}}$. The vertical dashed-dotted lines indicate the interval used for the alignment, while the vertical dashed lines mark the merger time. We find that while the (2, 2) and (4, 4) modes exhibit excellent agreement between the two waveforms, the (3, 2) mode shows larger discrepancies.

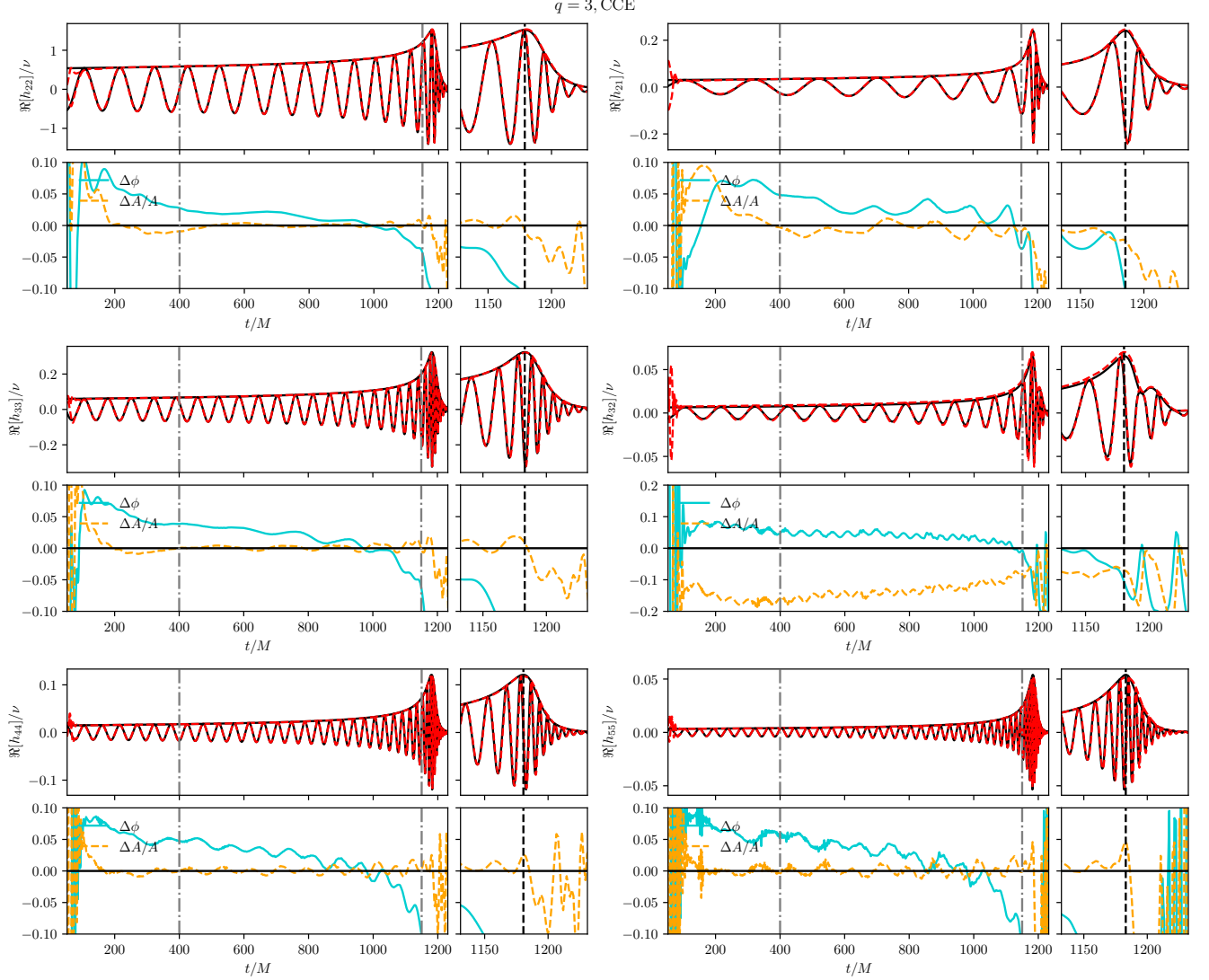


FIG. 20. Time domain comparison between the **GR-Athena++** (red dashed) and **SXS** (black) waveforms for the $(\ell, m) = \{(2, 2), (2, 1), (3, 3), (3, 2), (4, 4), (5, 5)\}$ modes and $q = 3$. Top panels show the real part of the waveform multipoles, while the bottom panels display the phase difference $\Delta\phi = \phi_{\ell m}^{\text{SXS}} - \phi_{\ell m}^{\text{GRA}}$ and the amplitude relative difference $\Delta A/A = 1 - A_{\ell m}^{\text{GRA}}/A_{\ell m}^{\text{SXS}}$. The vertical dashed-dotted lines indicate the interval used for the alignment, while the vertical dashed lines mark the merger time. Similarly to the $q = 1$ case, modes with $\ell = m$ – including the $(5, 5)$ mode – are in excellent agreement, while the $(3, 2)$ mode shows larger discrepancies.

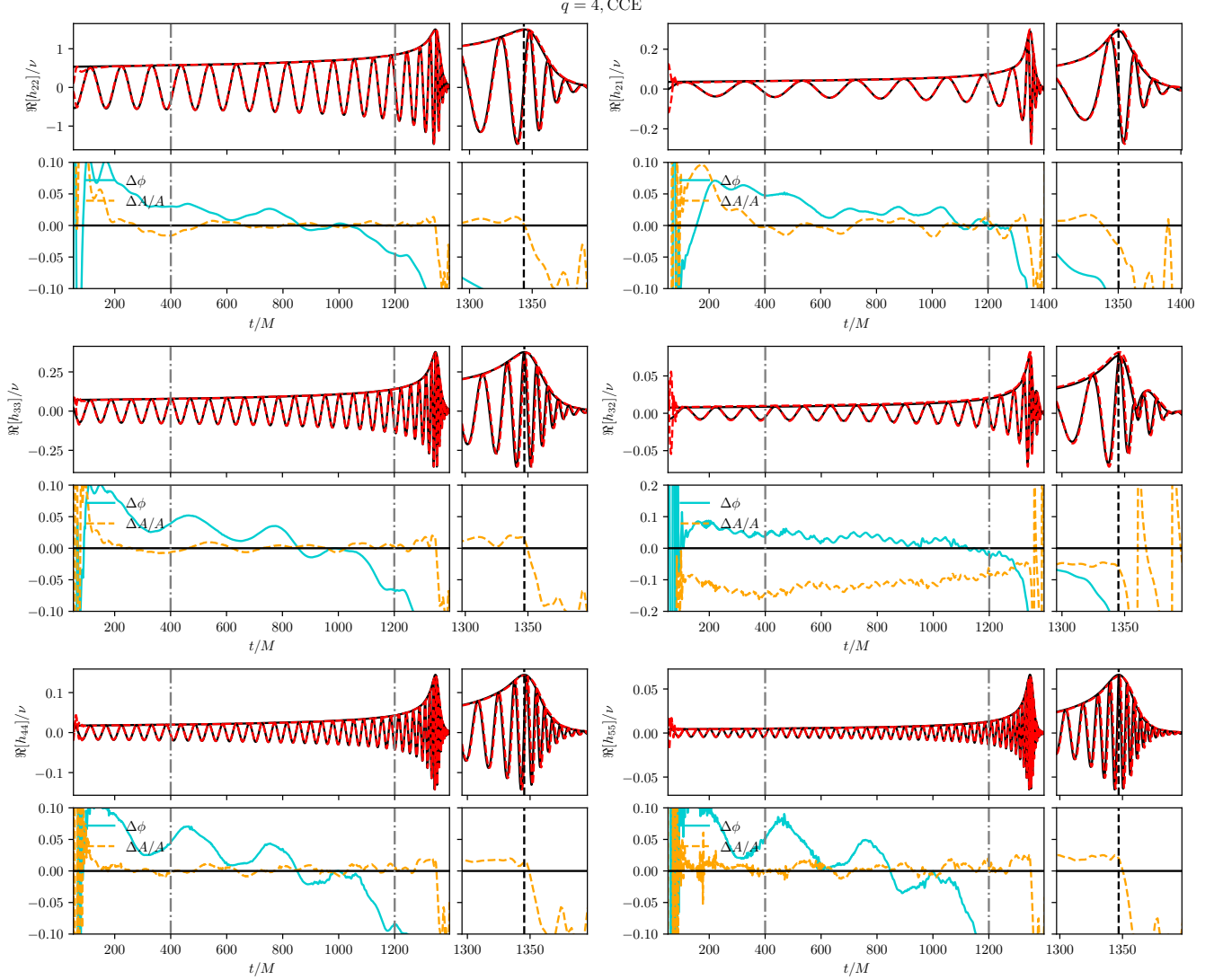


FIG. 21. Time domain comparison between the **GR-Athena++** (red dashed) and **SXS** (black) waveforms for the $(\ell, m) = \{(2, 2), (2, 1), (3, 3), (3, 2), (4, 4), (5, 5)\}$ modes and $q = 4$. Top panels show the real part of the waveform multipoles, while the bottom panels display the phase difference $\Delta\phi = \phi_{\ell m}^{\text{SXS}} - \phi_{\ell m}^{\text{GRA}}$ and the amplitude relative difference $\Delta A/A = 1 - A_{\ell m}^{\text{GRA}}/A_{\ell m}^{\text{SXS}}$. The vertical dashed-dotted lines indicate the interval used for the alignment, while the vertical dashed lines mark the merger time. Despite the lower resolution of the GRA waveforms with respect to other mass ratios (320 vs 384), the visual agreement and phase differences are comparable to those found with more refinement.

- [1] D. Radice and A. Rashti, *GR Athena:BHBH:0001*, <https://doi.org/10.26207/vnq9-za55> (2024).
- [2] D. Radice and A. Rashti, *GR Athena:BHBH:0002*, <https://doi.org/10.26207/ykyk-7b04> (2024).
- [3] D. Radice and A. Rashti, *GR Athena:BHBH:0003*, <https://doi.org/10.26207/yst7-9m47> (2024).
- [4] D. Radice and A. Rashti, *GR Athena:BHBH:0004*, <https://doi.org/10.26207/2rew-2b38> (2024).
- [5] F. Pretorius, Evolution of binary black hole spacetimes, *Phys. Rev. Lett.* **95**, 121101 (2005), [arXiv:gr-qc/0507014](https://arxiv.org/abs/gr-qc/0507014).
- [6] J. G. Baker, J. R. van Meter, S. T. McWilliams, J. Centrella, and B. J. Kelly, Consistency of post-Newtonian waveforms with numerical relativity, *Phys. Rev. Lett.* **99**, 181101 (2007), [arXiv:gr-qc/0612024](https://arxiv.org/abs/gr-qc/0612024).
- [7] M. Campanelli, C. O. Lousto, P. Marronetti, and Y. Zlochower, Accurate evolutions of orbiting black-hole binaries without excision, *Phys. Rev. Lett.* **96**, 111101 (2006), [arXiv:gr-qc/0511048](https://arxiv.org/abs/gr-qc/0511048).
- [8] S. G. Hahn and R. W. Lindquist, The two-body problem in geometrodynamics, *Annals of Physics* **29**, 304 (1964).
- [9] M. A. Scheel, H. P. Pfeiffer, L. Lindblom, L. E. Kidder, O. Rinne, and S. A. Teukolsky, Solving Einstein's equations with dual coordinate frames, *Phys. Rev. D* **74**, 104006 (2006), [arXiv:gr-qc/0607056](https://arxiv.org/abs/gr-qc/0607056).
- [10] U. Sperhake, Binary black-hole evolutions of excision and puncture data, *Phys. Rev. D* **76**, 104015 (2007), [arXiv:gr-qc/0606079](https://arxiv.org/abs/gr-qc/0606079).
- [11] B. Bruegmann, J. A. Gonzalez, M. Hannam, S. Husa, U. Sperhake, and W. Tichy, Calibration of Moving Puncture Simulations, *Phys. Rev. D* **77**, 024027 (2008), [arXiv:gr-qc/0610128](https://arxiv.org/abs/gr-qc/0610128).
- [12] B. Bruegmann, J. A. Gonzalez, M. Hannam, S. Husa, U. Sperhake, and W. Tichy, Calibration of Moving Puncture Simulations, *Phys. Rev. D* **77**, 024027 (2008), [arXiv:gr-qc/0610128](https://arxiv.org/abs/gr-qc/0610128).
- [13] B. Szilagyi, L. Lindblom, and M. A. Scheel, Simulations of Binary Black Hole Mergers Using Spectral Methods, *Phys. Rev. D* **80**, 124010 (2009), [arXiv:0909.3557](https://arxiv.org/abs/0909.3557) [gr-qc].
- [14] M. Thierfelder, S. Bernuzzi, and B. Bruegmann, Numerical relativity simulations of binary neutron stars, *Phys. Rev. D* **84**, 044012 (2011), [arXiv:1104.4751](https://arxiv.org/abs/1104.4751) [gr-qc].
- [15] F. Loffler *et al.*, The Einstein Toolkit: A Community Computational Infrastructure for Relativistic Astrophysics, *Class. Quant. Grav.* **29**, 115001 (2012), [arXiv:1111.3344](https://arxiv.org/abs/1111.3344) [gr-qc].
- [16] M. C. Babiuc, B. Szilagyi, J. Winicour, and Y. Zlochower, A Characteristic Extraction Tool for Gravitational Waveforms, *Phys. Rev. D* **84**, 044057 (2011), [arXiv:1011.4223](https://arxiv.org/abs/1011.4223) [gr-qc].
- [17] D. Hilditch, A. Weyhausen, and B. Brüggmann, Pseudospectral method for gravitational wave collapse, *Phys. Rev. D* **93**, 063006 (2016), [arXiv:1504.04732](https://arxiv.org/abs/1504.04732) [gr-qc].
- [18] M. Bugner, T. Dietrich, S. Bernuzzi, A. Weyhausen, and B. Brüggmann, Solving 3D relativistic hydrodynamical problems with weighted essentially nonoscillatory discontinuous Galerkin methods, *Phys. Rev. D* **94**, 084004 (2016), [arXiv:1508.07147](https://arxiv.org/abs/1508.07147) [gr-qc].
- [19] K. Clough, P. Figueras, H. Finkel, M. Kunesch, E. A. Lim, and S. Tunyasuvunakool, GRChombo : Numerical Relativity with Adaptive Mesh Refinement, *Class. Quant. Grav.* **32**, 245011 (2015), [arXiv:1503.03436](https://arxiv.org/abs/1503.03436) [gr-qc].
- [20] L. E. Kidder *et al.*, SpECTRE: A Task-based Discontinuous Galerkin Code for Relativistic Astrophysics, *J. Comput. Phys.* **335**, 84 (2017), [arXiv:1609.00098](https://arxiv.org/abs/1609.00098) [astro-ph.HE].
- [21] B. Daszuta, F. Zappa, W. Cook, D. Radice, S. Bernuzzi, and V. Morozova, GR-Athena++: Puncture Evolutions on Vertex-centered Oct-tree Adaptive Mesh Refinement, *Astrophys. J. Supp.* **257**, 25 (2021), [arXiv:2101.08289](https://arxiv.org/abs/2101.08289) [gr-qc].
- [22] A. Buonanno and T. Damour, Effective one-body approach to general relativistic two-body dynamics, *Phys. Rev. D* **59**, 084006 (1999), [arXiv:gr-qc/9811091](https://arxiv.org/abs/gr-qc/9811091).
- [23] A. Buonanno and T. Damour, Transition from inspiral to plunge in binary black hole coalescences, *Phys. Rev. D* **62**, 064015 (2000), [arXiv:gr-qc/0001013](https://arxiv.org/abs/gr-qc/0001013).
- [24] A. Ramos-Buades, A. Buonanno, M. Khalil, and S. Ossokine, Effective-one-body multipolar waveforms for eccentric binary black holes with nonprecessing spins, *Phys. Rev. D* **105**, 044035 (2022), [arXiv:2112.06952](https://arxiv.org/abs/2112.06952) [gr-qc].
- [25] L. Pompili *et al.*, Laying the foundation of the effective-one-body waveform models SEOBNRv5: Improved accuracy and efficiency for spinning nonprecessing binary black holes, *Phys. Rev. D* **108**, 124035 (2023), [arXiv:2303.18039](https://arxiv.org/abs/2303.18039) [gr-qc].
- [26] A. Ramos-Buades, A. Buonanno, H. Estellés, M. Khalil, D. P. Mihaylov, S. Ossokine, L. Pompili, and M. Shiferaw, Next generation of accurate and efficient multipolar precessing-spin effective-one-body waveforms for binary black holes, *Phys. Rev. D* **108**, 124037 (2023), [arXiv:2303.18046](https://arxiv.org/abs/2303.18046) [gr-qc].
- [27] D. Chiamello and A. Nagar, Faithful analytical effective-one-body waveform model for spin-aligned, moderately eccentric, coalescing black hole binaries, *Phys. Rev. D* **101**, 101501 (2020), [arXiv:2001.11736](https://arxiv.org/abs/2001.11736) [gr-qc].
- [28] S. Akçay, R. Gamba, and S. Bernuzzi, Hybrid post-Newtonian effective-one-body scheme for spin-precessing compact-binary waveforms up to merger, *Phys. Rev. D* **103**, 024014 (2021), [arXiv:2005.05338](https://arxiv.org/abs/2005.05338) [gr-qc].
- [29] R. Gamba, S. Akçay, S. Bernuzzi, and J. Williams, Effective-one-body waveforms for precessing coalescing compact binaries with post-Newtonian twist, *Phys. Rev. D* **106**, 024020 (2022), [arXiv:2111.03675](https://arxiv.org/abs/2111.03675) [gr-qc].
- [30] A. Nagar, P. Retegno, R. Gamba, S. Albanesi, A. Albertini, and S. Bernuzzi, Analytic systematics in next generation of effective-one-body gravitational waveform models for future observations, *Phys. Rev. D* **108**, 124018 (2023), [arXiv:2304.09662](https://arxiv.org/abs/2304.09662) [gr-qc].
- [31] A. Nagar, R. Gamba, P. Retegno, V. Fantini, and S. Bernuzzi, Effective-one-body waveform model for non-circularized, planar, coalescing black hole binaries: the importance of radiation reaction, (2024), [arXiv:2404.05288](https://arxiv.org/abs/2404.05288) [gr-qc].
- [32] A. Nagar, S. Bernuzzi, D. Chiamello, V. Fantini, R. Gamba, M. Panzeri, and P. Retegno, Effective-one-body waveform model for noncircularized, planar, co-

- alescing black hole binaries II: high accuracy by improving logarithmic terms in resummations, (2024), [arXiv:2407.04762 \[gr-qc\]](#).
- [33] P. Ajith *et al.*, Phenomenological template family for black-hole coalescence waveforms, *Class. Quant. Grav.* **24**, S689 (2007), [arXiv:0704.3764 \[gr-qc\]](#).
- [34] P. Ajith *et al.*, A Template bank for gravitational waveforms from coalescing binary black holes. I. Non-spinning binaries, *Phys. Rev. D* **77**, 104017 (2008), [Erratum: *Phys.Rev.D* 79, 129901 (2009)], [arXiv:0710.2335 \[gr-qc\]](#).
- [35] P. Ajith *et al.*, Inspiral-merger-ringdown waveforms for black-hole binaries with non-precessing spins, *Phys. Rev. Lett.* **106**, 241101 (2011), [arXiv:0909.2867 \[gr-qc\]](#).
- [36] L. Santamaria *et al.*, Matching post-Newtonian and numerical relativity waveforms: systematic errors and a new phenomenological model for non-precessing black hole binaries, *Phys. Rev. D* **82**, 064016 (2010), [arXiv:1005.3306 \[gr-qc\]](#).
- [37] S. Husa, S. Khan, M. Hannam, M. Pürrer, F. Ohme, X. Jiménez Forteza, and A. Bohé, Frequency-domain gravitational waves from nonprecessing black-hole binaries. I. New numerical waveforms and anatomy of the signal, *Phys. Rev. D* **93**, 044006 (2016), [arXiv:1508.07250 \[gr-qc\]](#).
- [38] S. Khan, S. Husa, M. Hannam, F. Ohme, M. Pürrer, X. Jiménez Forteza, and A. Bohé, Frequency-domain gravitational waves from nonprecessing black-hole binaries. II. A phenomenological model for the advanced detector era, *Phys. Rev. D* **93**, 044007 (2016), [arXiv:1508.07253 \[gr-qc\]](#).
- [39] G. Pratten, S. Husa, C. Garcia-Quiros, M. Colleoni, A. Ramos-Buades, H. Estelles, and R. Jaume, Setting the cornerstone for a family of models for gravitational waves from compact binaries: The dominant harmonic for nonprecessing quasicircular black holes, *Phys. Rev. D* **102**, 064001 (2020), [arXiv:2001.11412 \[gr-qc\]](#).
- [40] H. Estellés, A. Ramos-Buades, S. Husa, C. García-Quirós, M. Colleoni, L. Haegel, and R. Jaume, Phenomenological time domain model for dominant quadrupole gravitational wave signal of coalescing binary black holes, *Phys. Rev. D* **103**, 124060 (2021), [arXiv:2004.08302 \[gr-qc\]](#).
- [41] H. Estellés, M. Colleoni, C. García-Quirós, S. Husa, D. Keitel, M. Mateu-Lucena, M. d. L. Planas, and A. Ramos-Buades, New twists in compact binary waveform modeling: A fast time-domain model for precession, *Phys. Rev. D* **105**, 084040 (2022), [arXiv:2105.05872 \[gr-qc\]](#).
- [42] E. Hamilton, L. London, J. E. Thompson, E. Fauchon-Jones, M. Hannam, C. Kalaghatgi, S. Khan, F. Pannarale, and A. Vano-Vinuales, Model of gravitational waves from precessing black-hole binaries through merger and ringdown, *Phys. Rev. D* **104**, 124027 (2021), [arXiv:2107.08876 \[gr-qc\]](#).
- [43] L. London, S. Khan, E. Fauchon-Jones, C. García, M. Hannam, S. Husa, X. Jiménez-Forteza, C. Kalaghatgi, F. Ohme, and F. Pannarale, First higher-multipole model of gravitational waves from spinning and coalescing black-hole binaries, *Phys. Rev. Lett.* **120**, 161102 (2018), [arXiv:1708.00404 \[gr-qc\]](#).
- [44] C. García-Quirós, M. Colleoni, S. Husa, H. Estellés, G. Pratten, A. Ramos-Buades, M. Mateu-Lucena, and R. Jaume, Multimode frequency-domain model for the gravitational wave signal from nonprecessing black-hole binaries, *Phys. Rev. D* **102**, 064002 (2020), [arXiv:2001.10914 \[gr-qc\]](#).
- [45] S. Khan, F. Ohme, K. Chatziioannou, and M. Hannam, Including higher order multipoles in gravitational-wave models for precessing binary black holes, *Phys. Rev. D* **101**, 024056 (2020), [arXiv:1911.06050 \[gr-qc\]](#).
- [46] M. Hannam, P. Schmidt, A. Bohé, L. Haegel, S. Husa, F. Ohme, G. Pratten, and M. Pürrer, Simple Model of Complete Precessing Black-Hole-Binary Gravitational Waveforms, *Phys. Rev. Lett.* **113**, 151101 (2014), [arXiv:1308.3271 \[gr-qc\]](#).
- [47] P. Schmidt, F. Ohme, and M. Hannam, Towards models of gravitational waveforms from generic binaries II: Modelling precession effects with a single effective precession parameter, *Phys. Rev. D* **91**, 024043 (2015), [arXiv:1408.1810 \[gr-qc\]](#).
- [48] S. Khan, K. Chatziioannou, M. Hannam, and F. Ohme, Phenomenological model for the gravitational-wave signal from precessing binary black holes with two-spin effects, *Phys. Rev. D* **100**, 024059 (2019), [arXiv:1809.10113 \[gr-qc\]](#).
- [49] G. Pratten *et al.*, Computationally efficient models for the dominant and subdominant harmonic modes of precessing binary black holes, *Phys. Rev. D* **103**, 104056 (2021), [arXiv:2004.06503 \[gr-qc\]](#).
- [50] J. Blackman, B. Szilagyi, C. R. Galley, and M. Tiglio, Sparse Representations of Gravitational Waves from Precessing Compact Binaries, *Phys. Rev. Lett.* **113**, 021101 (2014), [arXiv:1401.7038 \[gr-qc\]](#).
- [51] J. Blackman, S. E. Field, M. A. Scheel, C. R. Galley, D. A. Hemberger, P. Schmidt, and R. Smith, A Surrogate Model of Gravitational Waveforms from Numerical Relativity Simulations of Precessing Binary Black Hole Mergers, *Phys. Rev. D* **95**, 104023 (2017), [arXiv:1701.00550 \[gr-qc\]](#).
- [52] V. Varma, S. E. Field, M. A. Scheel, J. Blackman, L. E. Kidder, and H. P. Pfeiffer, Surrogate model of hybridized numerical relativity binary black hole waveforms, *Phys. Rev. D* **99**, 064045 (2019), [arXiv:1812.07865 \[gr-qc\]](#).
- [53] V. Varma, S. E. Field, M. A. Scheel, J. Blackman, D. Gerosa, L. C. Stein, L. E. Kidder, and H. P. Pfeiffer, Surrogate models for precessing binary black hole simulations with unequal masses, *Phys. Rev. Research* **1**, 033015 (2019), [arXiv:1905.09300 \[gr-qc\]](#).
- [54] D. Williams, I. S. Heng, J. Gair, J. A. Clark, and B. Khamesra, Precessing numerical relativity waveform surrogate model for binary black holes: A Gaussian process regression approach, *Phys. Rev. D* **101**, 063011 (2020), [arXiv:1903.09204 \[gr-qc\]](#).
- [55] K. Chandra, V. Gayathri, J. C. Bustillo, and A. Pai, Numerical relativity injection analysis of signals from generically spinning intermediate mass black hole binaries in Advanced LIGO data, *Phys. Rev. D* **102**, 044035 (2020), [arXiv:2002.10666 \[astro-ph.CO\]](#).
- [56] J. Aasi *et al.* (LIGO Scientific, VIRGO, NINJA-2), The NINJA-2 project: Detecting and characterizing gravitational waveforms modelled using numerical binary black hole simulations, *Class. Quant. Grav.* **31**, 115004 (2014), [arXiv:1401.0939 \[gr-qc\]](#).
- [57] K. Chandra, A. Pai, V. Villa-Ortega, T. Dent, C. McIsaac, I. W. Harry, G. S. C. Davies, and K. Soni, Salient features of the optimised PyCBC IMBH search,

- in *16th Marcel Grossmann Meeting on Recent Developments in Theoretical and Experimental General Relativity, Astrophysics and Relativistic Field Theories* (2021) arXiv:2110.01879 [gr-qc].
- [58] J. Aasi *et al.* (LIGO Scientific), Advanced LIGO, *Class. Quant. Grav.* **32**, 074001 (2015), arXiv:1411.4547 [gr-qc].
- [59] D. Reitze *et al.*, Cosmic Explorer: The U.S. Contribution to Gravitational-Wave Astronomy beyond LIGO, *Bull. Am. Astron. Soc.* **51**, 035 (2019), arXiv:1907.04833 [astro-ph.IM].
- [60] M. Evans *et al.*, Cosmic Explorer: A Submission to the NSF MPSAC ngGW Subcommittee, (2023), arXiv:2306.13745 [astro-ph.IM].
- [61] M. Punturo *et al.*, The Einstein Telescope: A third-generation gravitational wave observatory, *Class. Quant. Grav.* **27**, 194002 (2010).
- [62] M. Maggiore *et al.*, Science Case for the Einstein Telescope, *JCAP* **03**, 050, arXiv:1912.02622 [astro-ph.CO].
- [63] P. Amaro-Seoane, H. Audley, S. Babak, J. Baker, E. Barausse, P. Bender, E. Berti, P. Binetruy, M. Born, D. Bortoluzzi, *et al.*, Laser interferometer space antenna, arXiv preprint arXiv:1702.00786 (2017).
- [64] J. Luo *et al.* (TianQin), TianQin: a space-borne gravitational wave detector, *Class. Quant. Grav.* **33**, 035010 (2016), arXiv:1512.02076 [astro-ph.IM].
- [65] Y.-L. Wu *et al.* (Taiji Scientific), China's first step towards probing the expanding universe and the nature of gravity using a space borne gravitational wave antenna, *Commun. Phys.* **4**, 34 (2021).
- [66] S. Kawamura *et al.*, The Japanese space gravitational wave antenna DECIGO, *Class. Quant. Grav.* **23**, S125 (2006).
- [67] P. Ajith *et al.*, The Lunar Gravitational-wave Antenna: Mission Studies and Science Case, (2024), arXiv:2404.09181 [gr-qc].
- [68] L. Lindblom, B. J. Owen, and D. A. Brown, Model Waveform Accuracy Standards for Gravitational Wave Data Analysis, *Phys. Rev. D* **78**, 124020 (2008), arXiv:0809.3844 [gr-qc].
- [69] V. Kapil, L. Reali, R. Costeta, and E. Berti, Systematic bias from waveform modeling for binary black hole populations in next-generation gravitational wave detectors, *Phys. Rev. D* **109**, 104043 (2024), arXiv:2404.00090 [gr-qc].
- [70] A. Dhani, S. Völkel, A. Buonanno, H. Estelles, J. Gair, H. P. Pfeiffer, L. Pompili, and A. Toubiana, Systematic Biases in Estimating the Properties of Black Holes Due to Inaccurate Gravitational-Wave Models, (2024), arXiv:2404.05811 [gr-qc].
- [71] K. Chandra, gwforge: A user-friendly package to generate gravitational-wave mock data, (2024), arXiv:2407.21109 [gr-qc].
- [72] M. Pürrer and C.-J. Haster, Gravitational waveform accuracy requirements for future ground-based detectors, *Phys. Rev. Res.* **2**, 023151 (2020), arXiv:1912.10055 [gr-qc].
- [73] A. Jan, D. Ferguson, J. Lange, D. Shoemaker, and A. Zimmerman, Accuracy limitations of existing numerical relativity waveforms on the data analysis of current and future ground-based detectors, *Phys. Rev. D* **110**, 024023 (2024), arXiv:2312.10241 [gr-qc].
- [74] D. Ferguson, K. Jani, P. Laguna, and D. Shoemaker, Assessing the readiness of numerical relativity for LISA and 3G detectors, *Phys. Rev. D* **104**, 044037 (2021), arXiv:2006.04272 [gr-qc].
- [75] P. Ajith *et al.*, The NINJA-2 catalog of hybrid post-Newtonian/numerical-relativity waveforms for non-precessing black-hole binaries, *Class. Quant. Grav.* **29**, 124001 (2012), [Erratum: *Class. Quant. Grav.* **30**, 199401 (2013)], arXiv:1201.5319 [gr-qc].
- [76] I. Hinder *et al.*, Error-analysis and comparison to analytical models of numerical waveforms produced by the NRAR Collaboration, *Class. Quant. Grav.* **31**, 025012 (2014), arXiv:1307.5307 [gr-qc].
- [77] A. Rashti, M. Bhattacharyya, D. Radice, B. Daszuta, W. Cook, and S. Bernuzzi, Adaptive mesh refinement in binary black holes simulations, *Class. Quant. Grav.* **41**, 095001 (2024), arXiv:2312.05438 [gr-qc].
- [78] S. Bernuzzi and D. Hilditch, Constraint violation in free evolution schemes: Comparing BSSNOK with a conformal decomposition of Z4, *Phys. Rev. D* **81**, 084003 (2010), arXiv:0912.2920 [gr-qc].
- [79] D. Hilditch, S. Bernuzzi, M. Thierfelder, Z. Cao, W. Tichy, and B. Bruegmann, Compact binary evolutions with the Z4c formulation, *Phys. Rev. D* **88**, 084057 (2013), arXiv:1212.2901 [gr-qc].
- [80] J. M. Stone, K. Tomida, C. J. White, and K. G. Felker, The athena++ adaptive mesh refinement framework: Design and magnetohydrodynamic solvers, *The Astrophysical Journal Supplement Series* **249** (2020).
- [81] M. J. Berger and J. Oliger, Adaptive Mesh Refinement for Hyperbolic Partial Differential Equations, *J. Comput. Phys.* **53**, 484 (1984).
- [82] M. Ansorg, B. Bruegmann, and W. Tichy, A Single-domain spectral method for black hole puncture data, *Phys. Rev. D* **70**, 064011 (2004), arXiv:gr-qc/0404056.
- [83] M. Hannam, S. Husa, F. Ohme, D. Muller, and B. Bruegmann, Simulations of black-hole binaries with unequal masses or nonprecessing spins: Accuracy, physical properties, and comparison with post-Newtonian results, *Phys. Rev. D* **82**, 124008 (2010), arXiv:1007.4789 [gr-qc].
- [84] A. Ramos-Buades, S. Husa, and G. Pratten, Simple procedures to reduce eccentricity of binary black hole simulations, *Phys. Rev. D* **99**, 023003 (2019), arXiv:1810.00036 [gr-qc].
- [85] N. T. Bishop, R. Gomez, L. Lehner, B. Szilagyi, J. Winicour, and R. A. Isaacson, Cauchy characteristic matching, in *Black Holes, Gravitational Radiation and the Universe: Essays in Honor of C.V. Vishveshwara*, edited by B. R. Iyer and B. Bhawal (1998) pp. 383–408, arXiv:gr-qc/9801070.
- [86] E.ourgoulhon, *3 + 1 Formalism in General Relativity*, July (Springer, Berlin New York, 2011).
- [87] C. Reisswig and D. Pollney, Notes on the integration of numerical relativity waveforms, *Class. Quant. Grav.* **28**, 195015 (2011), arXiv:1006.1632 [gr-qc].
- [88] L. F. Richardson, The Approximate Arithmetical Solution by Finite Differences of Physical Problems Involving Differential Equations, with an Application to the Stresses in a Masonry Dam, *Philosophical Transactions of the Royal Society A: Mathematical, Physical and Engineering Sciences* **210**, 307 (1911).
- [89] M. Alcubierre, *Introduction to 3+1 Numerical Relativity* (Oxford University Press, 2008).
- [90] D. R. Brill, On the positive definite mass of the Bondi-Weber-Wheeler time-symmetric gravitational waves,

- Annals Phys.* **7**, 466 (1959).
- [91] W. Tichy, A. Rashti, T. Dietrich, R. Dudi, and B. Brügmann, Constructing binary neutron star initial data with high spins, high compactnesses, and high mass ratios, *Phys. Rev. D* **100**, 124046 (2019), [arXiv:1910.09690 \[gr-qc\]](#).
- [92] H. P. Pfeiffer, D. A. Brown, L. E. Kidder, L. Lindblom, G. Lovelace, and M. A. Scheel, Reducing orbital eccentricity in binary black hole simulations, *Class. Quant. Grav.* **24**, S59 (2007), [arXiv:gr-qc/0702106](#).
- [93] I. Harry, J. Calderón Bustillo, and A. Nitz, Searching for the full symphony of black hole binary mergers, *Phys. Rev. D* **97**, 023004 (2018), [arXiv:1709.09181 \[gr-qc\]](#).
- [94] K. Chandra, J. Calderón Bustillo, A. Pai, and I. W. Harry, First gravitational-wave search for intermediate-mass black hole mergers with higher-order harmonics, *Phys. Rev. D* **106**, 123003 (2022), [arXiv:2207.01654 \[gr-qc\]](#).
- [95] P. Amaro-Seoane *et al.* (LISA), Laser Interferometer Space Antenna, (2017), [arXiv:1702.00786 \[astro-ph.IM\]](#).
- [96] B. Vaishnav, I. Hinder, F. Herrmann, and D. Shoemaker, Matched filtering of numerical relativity templates of spinning binary black holes, *Phys. Rev. D* **76**, 084020 (2007), [arXiv:0705.3829 \[gr-qc\]](#).
- [97] S. Babak, A. Petiteau, and M. Hewitson, LISA Sensitivity and SNR Calculations, (2021), [arXiv:2108.01167 \[astro-ph.IM\]](#).
- [98] L. T. Buchman, H. P. Pfeiffer, M. A. Scheel, and B. Szilágyi, Simulations of non-equal mass black hole binaries with spectral methods, *Phys. Rev. D* **86**, 084033 (2012), [arXiv:1206.3015 \[gr-qc\]](#).
- [99] J. Blackman, S. E. Field, C. R. Galley, B. Szilágyi, M. A. Scheel, M. Tiglio, and D. A. Hemberger, Fast and Accurate Prediction of Numerical Relativity Waveforms from Binary Black Hole Coalescences Using Surrogate Models, *Phys. Rev. Lett.* **115**, 121102 (2015), [arXiv:1502.07758 \[gr-qc\]](#).
- [100] M. Boyle *et al.*, The SXS Collaboration catalog of binary black hole simulations, *Class. Quant. Grav.* **36**, 195006 (2019), [arXiv:1904.04831 \[gr-qc\]](#).
- [101] A. Albertini, A. Nagar, P. Rettengo, S. Albanesi, and R. Gamba, Waveforms and fluxes: Towards a self-consistent effective one body waveform model for non-precessing, coalescing black-hole binaries for third generation detectors, *Phys. Rev. D* **105**, 084025 (2022), [arXiv:2111.14149 \[gr-qc\]](#).
- [102] D. Ferguson *et al.*, Second MAYA Catalog of Binary Black Hole Numerical Relativity Waveforms, (2023), [arXiv:2309.00262 \[gr-qc\]](#).
- [103] J. Moxon, M. A. Scheel, S. A. Teukolsky, N. Deppe, N. Fischer, F. Hébert, L. E. Kidder, and W. Thrope, SpECTRE Cauchy-characteristic evolution system for rapid, precise waveform extraction, *Phys. Rev. D* **107**, 064013 (2023), [arXiv:2110.08635 \[gr-qc\]](#).
- [104] E. Newman and R. Penrose, An Approach to gravitational radiation by a method of spin coefficients, *J. Math. Phys.* **3**, 566 (1962).
- [105] C. O. Lousto, H. Nakano, Y. Zlochower, and M. Campanelli, Intermediate-mass-ratio black hole binaries: Intertwining numerical and perturbative techniques, *Phys. Rev. D* **82**, 104057 (2010), [arXiv:1008.4360 \[gr-qc\]](#).
- [106] K. Kiuchi, K. Kawaguchi, K. Kyutoku, Y. Sekiguchi, M. Shibata, and K. Taniguchi, Sub-radian-accuracy gravitational waveforms of coalescing binary neutron stars in numerical relativity, *Phys. Rev. D* **96**, 084060 (2017), [arXiv:1708.08926 \[astro-ph.HE\]](#).
- [107] S. Albanesi, A. Rashti, F. Zappa, R. Gamba, W. Cook, B. Daszuta, S. Bernuzzi, A. Nagar, and D. Radice, Scattering and dynamical capture of two black holes: synergies between numerical and analytical methods, (2024), [arXiv:2405.20398 \[gr-qc\]](#).